Artificial Neural Network Methods for Lithium-Ion Battery Behavior Predictions

by

Gyouho Cho

A dissertation submitted in partial fulfillment
of the requirements for the degree of
Doctor of Philosophy
(Electrical and Computer Engineering)
in the University of Michigan-Dearborn
2022

Doctoral Committee:

Associate Professor Mengqi Wang, Chair
Assistant Professor Youngki Kim
Assistant Professor Jaerock Kwon
Associate Professor Wencong Su

Dedication

To my loving family

and

my friends in Ford Motor Company

Acknowledgements

First and foremost, I would like to express the deepest gratitude to my Ph.D. advisor, Prof. Mengqi Wang, who has provided me guidance and encouragement since the beginning of my Ph.D. program. It has been a great pleasure having an opportunity to work with her.

Also, I am thankful to my committee members, Jaerock Kwon, Youngki Kim, and Wencong Su, for providing technical feedback and advice on my research. I truly appreciate their time and effort to guide my Ph.D. work.

Furthermore, I would like to express my appreciation to Dr. Di Zhu and Jeffrey Joseph Campbell from Ford Motor Company for providing technical advice regarding neural network methods and lithium-ion batteries and for sharing the battery test data. I thank them for their time and support on my Ph.D. work.

Lastly, my sincere thanks also go to Ford Motor Company for providing an opportunity and financial support to enroll in this Ph.D. program.

Table of Contents

List of Tables

List of Figures

Abstract

The lithium-ion battery is a significant component in systems where electrification has been applied to achieve sustainability goals, such as electrical vehicles fulfilling emissions requirements. In order to control the lithium-ion battery to attain the safety, reliability, and performance demands of the electrified devices while maintaining design specifications, accurate predictions of the battery behaviors are essential.

Data-driven methods with the recent technological breakthroughs in machine learning are regarded as solutions to characterize and simulate battery behaviors such as lithium-ion battery voltage and temperature. Long short-term memory (LSTM), a type of recurrent neural network (RNN), shows accurate battery behavior prediction compared with other data-driven methods in the literature. To predict the lithium-ion cell voltage at a low temperature and to estimate the temperature distribution of the lithium-ion battery pack, the LSTM architectures are designed and trained with lithium-ion battery cell and pack test data. This data-driven method shows high accuracy, convergency, and robustness against external variables such as ambient temperature variation. However, the highly data-oriented nature of the LSTM method struggles with increased prediction error when local data deficiency occurs. In the case of pack temperature estimation, the effect of data scarcity is evidenced by differentiating the input temperature geometry (at the edge of the battery module) from the predicted temperature location (middle of the battery module). To solve this drawback of the data-driven method, the physics-informed

neural network (PINN) is developed to provide an additional source, physics law, for training the data-driven method.

The PINN model to predict the battery cell temperature is developed by applying the battery thermal model to the loss function, implementing adaptive coefficients to the loss function, and modifying the neural network architecture with the pre-layer and connection layer, reflecting the analytical solution of the battery thermal model. The developed PINN model is superior in predicting the lithium-ion battery cell temperature with limited data size and an unidentified battery thermal model. This PINN model was applied to the aforementioned LSTM architecture to enhance the battery pack temperature estimation. The proposed LSTM-PINN hybrid model has more accurate predictions than the LSTM model proposed when data scarcity occurs. Furthermore, the LSTM-PINN hybrid model shows robustness against the incompleteness of the battery thermal model.

In addition to predicting lithium-ion battery behavior, the data-driven method could be applied to lithium-ion battery model identifications. Various neural network methods are applied in the literature to find the battery model coefficients. However, most studies implement the full factorial design of experiment method for the data sampling from the simulation data created by the battery model. This data sampling approach induces a large data size and limits the number of identified battery model parameters. To improve this drawback of the full factorial data sampling method, Plackett-Burman (PB), Latin hypercube (LH), and PB/LH combined methods are applied to identify the eight battery model parameters from the pseudo-two-dimensional

(P2D) lithium-ion model. The LH sampling method reduces the data size by more than 90% while keeping the prediction error increase manageable (3% increase).

Chapter 1 Introduction

1.1 Motivation

Global warming has caught recent public attention since it creates environmental and social issues such as ecological imbalance, economic crisis, and political conflicts. Among many factors causing global warming, greenhouse gases such as carbon dioxide are considered the primary driver [1]. Furthermore, according to studies like the one done by Heede et al., the majority of global carbon emissions are due to human activities such as vehicle transportation and power generation [2]. Therefore, human activities are critical factors in easing global warming. Recent movements in the electrification of transportation by vehicle manufacturers are part of the social efforts to separate human activities from greenhouse gas emissions to avoid global warming.

The lithium-ion battery is an energy storage device that converts electrical energy to chemical energy during charging. Then it converts the chemical energy to electrical energy during discharge under a load. Lithium ions migrate between the anode and cathode during the lithium-ion battery's operation while electrons flow to an external load. Fig. 1 shows a simplified schematic illustrating the battery operation, and Table 1 shows the material information of each lithium-ion battery component.

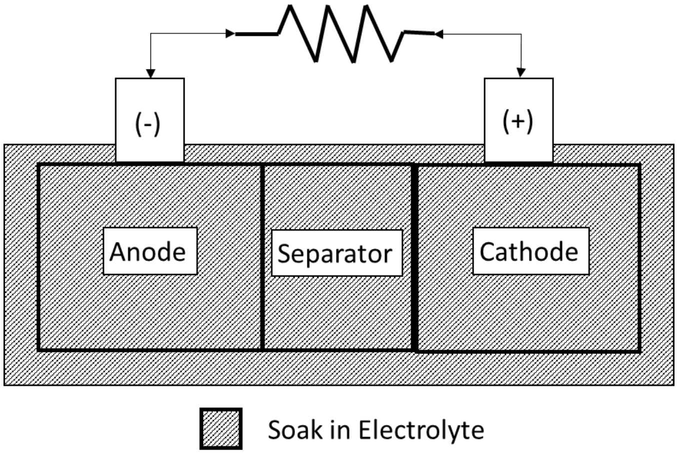

Fig. 1 Lithium-ion battery operation

Table 1 Lithium-ion battery components and material information

Component	Material
Anode	Carbon or Silicon compounds
Cathode	Transitional metal oxides
Separator	Polymer
Electrolyte	Carbonate solvent + Li salt
Anode foil	Copper
Cathode foil	Aluminum
Case	Aluminum base

Since the commercialization of the lithium-ion battery in 2005, portable electronic devices have used the lithium-ion battery as the energy storage source [3]. In recent lithium-ion battery design, transition metal alloys containing cobalt, nickel, and manganese are synthesized to work as the cathode. Carbon compounds such as graphite are used as anodes to boost energy density [4]. With this technical breakthrough in chemistry to improve the performance, the lithium-ion battery is also regarded as the primary energy storage device for vehicle electrification. Major automotive companies have introduced hybrid [5–7] and full electrical vehicles with high-energy lithium-ion battery systems [8]. Table 2 shows the commercially available hybrid and electric vehicles with their battery specifications. These new types of electrified transportation with lithium-ion batteries will either reduce or eliminate greenhouse gas emissions.

Table 2 Lithium-ion battery chemistry and energy of electrical vehicles [9]

Vehicle	Chemistry	Usable Battery Energy (kWh)
Mercedes EQS	NMC	107.8
Tesla X and Tesla S	NCA	95
Ford Mustang Mach-E	NMC	91
Audi e-tron	NMC	86.5
Volkswagen ID.5	NMC	77
Hyundai IONIQ 5	NMC	72.5

(N = Nickel, M=Manganese, C=Cobalt and A = Aluminium)

Despite the advantages of the lithium-ion battery, such as high energy density, minimal memory effect, and relatively wide operation temperature ranges [10, 11], it has short life and safety risks when it operates out of its operating voltage and temperature ranges [12]. Any lithium-ion battery operations under the low operation temperature limit degrade the battery performance. Any operations over the high operation temperature limit induce hazardous events such as thermal runaway or explosion [13–15]. To avoid this catastrophic failure that the lithium-ion battery may face, the battery management system (BMS) should be capable of estimating the battery state parameters such as state of charge (SOC) and state of health (SOH) and predicting the battery behaviors such as battery voltage and temperature. However, the nonlinear characteristics of the lithium-ion battery make it difficult for BMS to anticipate the battery behavior, potentially leading to poor battery control [16]. Therefore, accurate and reliable methods to model and estimate the lithium-ion battery behavior are necessary for enhancing the battery usage by improving the battery safety and life. Also, this improvement will lead to further electrification of transportation to reduce greenhouse gas emissions. This dissertation conducts a series of studies to implement artificial neural network-based methods.

1.2 Artificial Neural Network

Since Hinton and co-researchers' technical breakthrough with an artificial neural network (ANN) and deep learning, introduced in their research papers [17–18], ANN has been successfully applied to a broad range of areas such as pattern recognition [19–20], natural language processing [21–22], portfolio management [23–24], medical diagnosis [25–26], and financial forecasting [27–28]. In these applications, ANN performs three major types of tasks. In the supervised learning task, ANN models the input and output relationship. Then the trained ANN predicts the outputs for any given inputs. In the unsupervised learning task, ANN is trained to perform the clustering, filtering, and estimating of input data distribution [29]. In the reinforced force learning task, ANN is trained to minimize the cost function, guiding the agent's behavior for optimum control [30]. An application such as the lithium-ion battery behavior estimation that will be discussed in this dissertation paper falls under the supervised learning task category.

ANN consists of multiple artificial neurons (AN) that resemble the functions of the biological neurons that are the basic units of the human brain. As shown in Fig. 2, the input signal is provided to the AN. Then the AN processes the input signal and transmits the output signal. AN conducts the signal processing by mathematical calculation with the weight, bias, and activation function. The mathematical formulation for the signal process is given in (1) [31].

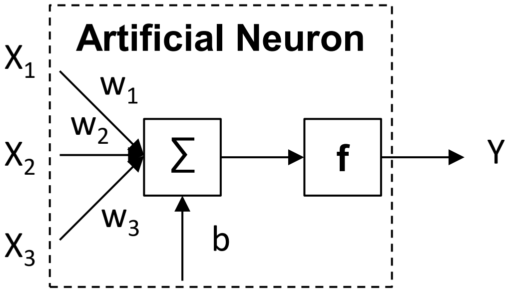

Fig. 2 Artificial Neuron
(X: input, W: weight, b: bias, f: activation function and Y: output) [31]

$$Y_j = f\left(\sum_i W_{ij} \cdot X_i + b\right) \tag{1}$$

In (1), Y is the j^{th} output of a neuron, f is the activation function, W_{ij} is the weight between the i^{th} input and the j^{th} output, X_i is the i^{th} input, and b is the bias. Typical activation functions implemented in ANN are provided in Table 3.

Table 3 List of the activation functions [32]

Name	**Equation**	**Range**
Linear	$f(x) = x$	(-infinity to infinity)
Sigmoid	$f(x) = \frac{1}{1 + e^{-x}}$	(0 to 1)
Hyperbolic tangent (tanh)	$f(x) = \tanh(x)$	(-1 to 1)
Rectified linear unit (ReLU)	$f(x) = 0 \; for \; x < 0$ $f(x) = x \; for \; x \geq 0$	(0 to infinity)
Exponential linear unit (ELU)	$f(x) = \alpha(e^x - 1) for \; x < 0$ $f(x) = x \; for \; x \geq 0$	(-1 to infinity)

During the training process, the prediction accuracy of ANN is optimized by using backpropagation with a loss function. Table 4 shows the typical loss functions applied to the supervised learning tasks. Also, the ANN implements multiple hidden layer structures to take a deep learning approach, as in Fig. 3. This deep neural network is known for its strength in accurately predicting problems with nonlinearity, such as fluid dynamics [33] and electromagnetics [34].

Table 4 List of the loss functions [35]

Name	Equation
Mean Square Error	$MSE = \frac{\sum_{i=1}^{n}(y_i - \hat{y}_i)^2}{n}$
Mean Absolute Error	$MAE = \frac{\sum_{i=1}^{n}\lvert y_i - \hat{y}_i \rvert}{n}$
Mean Bias Error	$MBE = \frac{\sum_{i=1}^{n}(y_i - \hat{y}_i)}{n}$

(n= sample number, y_i = true value and $\hat{y}_i$ = output from ANN)

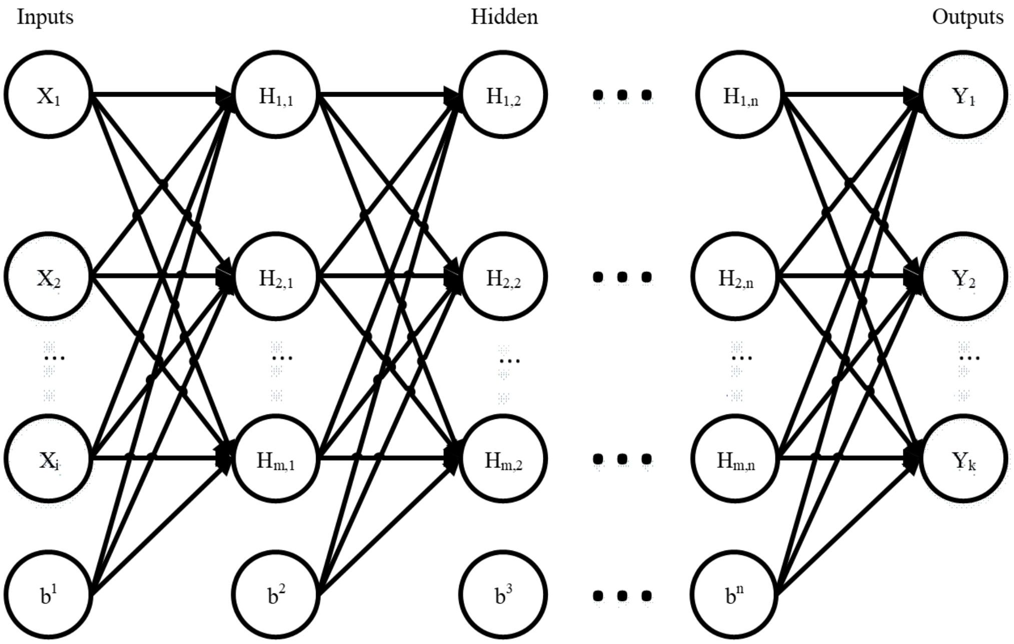

Fig. 3 Deep Neural Network (multiple hidden layers) [31]

With its characteristics, especially its strength in learning nonlinearity, ANN is a suitable data-driven method to estimate lithium-ion battery performance parameters and behaviors. The following subsections of this paper contain a review of the recently published studies implementing ANN to estimate SOC, SOH, battery voltage, and battery temperature.

1.2.1 Artificial Neural Network for SOC Estimation

The lithium-ion battery SOC is the ratio of residual capacity to installed capacity as formulated in (2). SOC works as a gauge indicating the amount of the charged energy available in the lithium-ion battery. SOC is significant to lithium-ion battery control because SOC is related not only to the time left to empty the battery energy but also to the battery performance such as battery power and the battery safety by avoiding overcharge and overdischarge.

$$SOC = \frac{Q_{residual}}{Q_{Installed}} \cdot 100\% \tag{2}$$

In (2), $Q_{residual}$ and $Q_{Installed}$ represent the residual capacity and the installed capacity, respectively.

In the literature, ANN has been applied to predict the SOC of the lithium-ion battery in a supervised learning task manner such that the input measurements are fed into the ANN and the ANN predicts the SOC of the lithium-ion battery as the output of the ANN. In [35], the authors implemented a one input layer, one hidden layer, and one output layer structure for the ANN with backpropagation. In [36], the authors applied the ANN method as in the previous literature but with multiple hidden layers with the ADAM customized method to update the weights and bias of the ANN. In studies [37] and [38], the ANN methods with multiple hidden layers were implemented with the backtracking search algorithm (BSA) and particle swarm optimization (PSA) to optimize the neuron number and learning rate of the ANN to avoid either overfitting or underfitting while training the ANN. In [39], the authors modified the ANN structure to become a recurrent neural network (RNN). RNN is another form of ANN in which the output of the previous sequence is fed to the ANN as the input. This paper applies the nonlinear autoregressive exogenous (NARX) method to the ANN to make it an RNN. Table 5 summarizes the SOC estimation errors of the reviewed ANN methods. The prediction error summary table shows that most ANN methods have less than 1% prediction error. Also, it is noticeable that the RNN method has the lowest prediction error even at a low temperature. This outcome is expected since the battery data are mostly time-series data, and the RNN can learn the previous event information.

Table 5 SOC estimation error from the literatures

Neural Network Architecture	RMSE	MAE	Temperature
ANN [35]	0.20 %	-	25°C
ANN with ADAM [36]	0.78 %	0.61 %	-20 to 25°C
MLP with BSA [37]	0.57 %	0.38 %	25°C
MLP with BSA and PSO [38]	1.37 %	1.01 %	25°C
RNN [39]	0.30 %	-	0 °C

1.2.2 Artificial Neural Network for SOH Estimation

The lithium-ion battery is degraded over time by cycle and calendar effects. SOH is a parameter that shows the progress of lithium-ion battery degradation. The battery SOH is the ratio of maximum capacity to installed capacity as formulated in (3).

$$SOH = \frac{Q_{max}}{Q_{Installed}} \cdot 100\% \tag{3}$$

In (3), Q_{max} is the maximum capacity and $Q_{Installed}$ is the installed capacity.

Like the SOC estimation, most research studies applied ANN to predict the SOH of the lithium-ion battery in a supervised learning fashion such that the input measurements and battery state parameters are fed into the ANN and the ANN then predicts the SOH of the lithium-ion batteryas the output. In [40], the structure of the ANN used in the study has one input layer, one hidden layer, and one output layer. For the inputs to the ANN, SOC and three battery model parameters are fed to the ANN. In [41], the study implements an ANN consisting of one input layer, two hidden layers, and one output layer, with the numbers of neurons in each layer being 10, 7, 4, and 1. Also, in this study, the autoencoder neural network, a subcategory of the ANN, is applied to the battery data to perform the feature extraction. Then, the autoencoder neural network outputs are fed to the ANN structure. In [42], the structure of the ANN contains one input layer, one hidden layer, and one output layer. The battery current, voltage, and SOC are fed to the input layer in the input layer. This paper has the battery capacity as the output from the ANN. Also, this paper created RNN by inserting the battery capacity of the previous time sequence into the input layer. In addition to [42], many studies are using RNN. In [39], the RNN structure developed with NARX is also applied to predict the SOH. In [43], the RNN structure is introduced by adding the capacity and resistance impedance spectroscopy measurements of the previous time sequence. This structure predicts the capacity and resistance impedance spectroscopy measurements of the future time sequence for the output. Table 6 summarizes the SOH estimation errors of the reviewed ANN methods. This literature review found that the RNN structure had a more accurate prediction than the ANN without the previous sequence information in the input layer.

Table 6 SOH estimation error from the literature

Neural Network Architecture	RMSE	MAE
ANN [40]	-	7.2%
ANN with Autoencoder [41]	6.66%	-
ANN [42]	4.72%	-
RNN [39]	0.1%	-
RNN [42]	0.41%	-
RNN [43]	0.46	-

1.2.3 Artificial Neural Network for Predicting Lithium-Ion Battery Voltage

Battery voltage is a response of the lithium-ion battery continuously measured by the battery management system (BMS). Battery voltage influences the lithium-ion battery's cost, safety, and performance. For instance, a lithium-ion battery with a nickel, cobalt, and manganese composite cathode has a battery operation voltage range between 2.5V and 4.1V. Any battery voltage operation away from this range causes battery overcharge and discharge, which will be the root cause of hazardous phenomena such as thermal runaway [44]. In addition to the lithium-ion battery safety aspect, the battery voltage is also essential to estimating lithium-ion battery characterization parameters such as SOC and SOH. Also, the system-level rule-based [45] and optimization-based [46] battery management strategies require high accuracy for the battery voltage prediction. Therefore, battery voltage prediction influences battery control, which is related to lithium-ion battery performance and battery cost since with high confidence in the battery control the design margin could be eliminated [44].

In the published studies, RNN and its relative structures, such as gated recurrent unit (GRU) and long-short term memory (LSTM), are applied mainly to predict the lithium-ion battery voltage. This implementation of the RNN is due to the time series characteristics of the battery data and the high prediction accuracy of the RNN with the battery data, as reviewed in the two previous sections regarding SOC and SOH. In [47], the authors developed particular RNN architectures, GRU and LSTM, to predict the lithium-ion battery voltage. In this design, the current, amp-hour counting, temperature, and voltage at the previous time sequence were fed to the RNN architecture to predict the battery voltage at the current time sequence. In both cases, the absolute voltage prediction error was less than 10% for 25°C, 10°C, and -10°C. In [48], the study proposed another LSTM architecture to predict the battery voltage. In this method, the inputs to the LSTM model are the battery voltage, SOC, brake pedal stroke value, and vehicle speed at the previous time sequence.

Moreover, the output is the battery voltage at the current time sequence. The reported battery voltage prediction error (relative error) was less than 1% at a temperature range between 0 and 10°C. Finally, in [49], the authors proposed an LSTM model combined with the lithium-ion equivalent circuit model. In this method, the inputs to the LSTM model were the cell voltage, pack voltage, and pack SOC in the previous time sequence. Furthermore, the output was the battery cell voltage at the current time sequence. The proposed LSTM had a prediction error (mean square error) of less than 0.01%.

In summary, the proposed ANN models in the literature, mainly RNN architectures, successfully predicted the lithium-ion voltage with high accuracy. However, there are some limitations in the studies found in the literature. First, since every study used a different prediction error definition, comparing the proposed RNN models is challenging. So, it is not possible to rank the proposed methodologies. One of the significant challenges in lithium-ion battery voltage is its prediction at low temperatures. However, in the literature, the lowest temperature the proposed models validated was -10°C, which is a modest low temperature. The lithium-ion battery for transportation requires cold cranking at extremely low temperatures, e.g., -30°C [50]. In chapter II of this dissertation paper, these shortcomings in the literature will be revisited by conducting a comparison study among various types of RNN at a low temperature of -30°C.

1.2.4 Artificial Neural Network for Predicting Battery Temperature

Battery temperature is another continuously measured response of the lithium-ion battery, which is essential for battery management since the battery temperature influences the lithium-ion battery's safety and performance. The lithium-ion battery has outstanding performance in terms of efficiency and safety in the temperature range between 20°C and 40°C [51]. The lithium-ion battery suffers from performance degradation at low temperatures because of the high internal resistance. Also, high temperatures may lead to safety concerns such as thermal runaway [52]. However, the physical and cost constraints in lithium-ion battery design limit the number of temperature sensors in the lithium-ion battery pack. Due to this scarcity of temperature information, especially in large batteries, lithium-ion battery temperature prediction is necessary to control lithium-ion battery usage to avoid undesired battery temperature and to develop the battery structure and cooling and heating methods.

In the literature, as with lithium-ion battery SOC, SOH, and voltage predictions, RNN architectures are popular ANN structure choices to predict the battery temperature. In [53], the authors compared various ANN and LSTM structures to predict the battery surface temperature. In this study, various combinations of the inputs were studied with the two neural network structures. The input variables considered in this study were the battery current, voltage, SOC, ambient temperature, filtered battery current, and voltage. In the results, the lowest ANN prediction error (root mean square error) was 1.3 °C, and the lowest LSTM prediction error was 0.7 °C. The authors also concluded that LSTM had a better prediction accuracy than ANN for all cases reviewed in the paper. In [54], the authors implemented the GRU architecture alone to predict the core lithium-ion battery temperature. In the GRU model, battery voltage, current, ambient temperature, and battery surface temperature were fed to the GRU model. The output was the core battery temperature. This GRU model's prediction error (maximum absolute error) was 0.066 °C. In this dissertation paper, an LSTM structure will be developed to predict large battery pack temperatures at various locations in the battery pack.

1.2.5 Advantages and Disadvantages of Artificial Neural Networks

The literature review shows that the ANN-based methods have advantages in battery behavior prediction. First, the ANN-based predictions have high accuracy, primarily when structured as an RNN-based architecture. In the study included in [55], the RNN-based method had better prediction accuracy than the model-based method, with one order of magnitude lower prediction error (mean square error). Second, the ANN method does not require system identification. The battery model needs to be identified in order for the model-based method to make the battery behavior prediction. However, accurate battery model identification is not always available and is challenging for modeling lithium-ion battery behavior.

Despite the advantages, the ANN method has drawbacks, mainly related to training data availability and quality. This drawback is because the learning process is based solely on the training data. Lithium-ion battery test data derived mainly from the large-sized lithium-ion battery packs for electric cars are costly to produce, and therefore the data availability is limited. This dissertation proposes a physics-informed neural network (PINN) methodology to improve on the high dependency of ANN methods on the training data. Related works will be discussed in the later sections of this dissertation paper.

1.2.6 RNN Methods

1.2.6.1 Simple RNN (Recurrent Neural Network)

Simple RNN is the simplest recurrent neural network structure, which resembles the feed-forward ANN in which the inputs and bias apply to the activation function in the hidden layer to produce the outputs. However, the simple RNN connects the input and output [56]. Fig. 4 presents a unit cell of the simple RNN without the rolled-through time representation. The figure indicates the connection between the input and output by the brown loop allowed in the hidden layer.

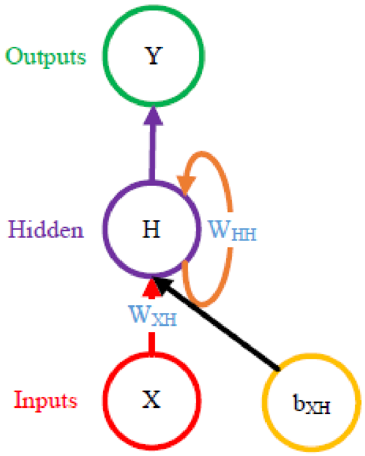

Fig. 4 Simple RNN unit cell [57]

The output of the simple RNN is also formulated as below.

$$Y(t) = \sigma(W_{XH}X_t + W_{HH}H_{t-1} + b_{XH}) \tag{4}$$

In the equation, $Y(t)$ is the output at time t. σ is the activation function. X_t is the input at the time t. W_{XH} is the weight between the input and the hidden layer. W_{HH} is the weight for the hidden layer. $H_{t-1}$is the output from the hidden layer at time t - 1 (past). b_{XH} is the bias [56].

Furthermore, throughout the sequence data, the recurring weight, W_{HH}, is updated by recurrently multiplying the recurring weight. Since this process involves the same number multiplication multiple times, based on the magnitude of the recurring weight, the updated weight could either vanish out for a small number or explode for a large number. This change is the vanish gradient problem of the RNN. This problem is a phenomenon that needs to be managed during the implementation of the RNN. Following, two RNN methods are developed to avoid the vanish gradient problem.

1.2.6.2 LSTM (Long Short-Term Memory)

LSTM is a type of neural network that belongs to the recurrent neural network (RNN) family. Indeed, LSTM can overcome the vanishing gradient challenge that RNN suffers while updating its weights. This improvement is due to the long-term state memory and associated layer structures included in the architecture. A unit cell of LSTM consists of four different layers. The main layer acts like an RNN but with a long-term state memory. A forget gate layer removes the undesired portion of the long-term state memory. An input gate layer directs a portion of the output to the long-term state memory. Lastly, an output gate selects a portion of the long-term state memory to the output [56]. Fig. 5 shows an LSTM unit cell followed by a list of the equations formulated in the LSTM.

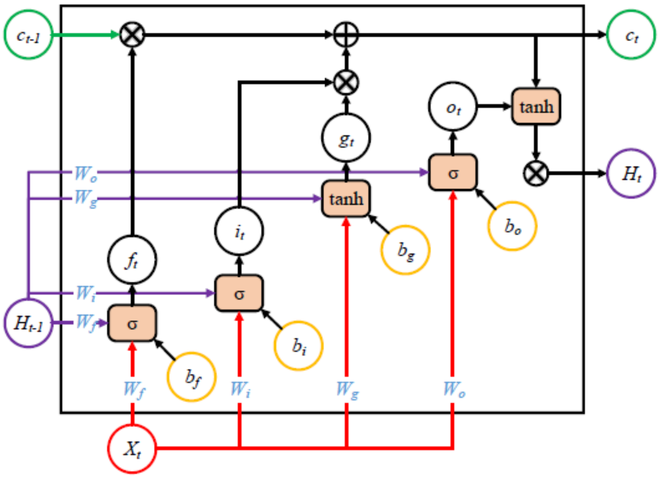

Fig. 5 LSTM unit cell [57]

$$f(t) = \sigma(W_f X_t + W_f H_{t-1} + b_f) \tag{5}$$

$$i(t) = \sigma(W_i X_t + W_i H_{t-1} + b_i) \tag{6}$$

$$g(t) = tanh(W_g X_t + W_g H_{t-1} + b_g) \tag{7}$$

$$o(t) = \sigma(W_o X_t + W_o H_{t-1} + b_o) \tag{8}$$

$$c(t) = f(t) \otimes c(t-1) + i(t) \otimes g(t) \tag{9}$$

$$h(t) = o(t) \otimes tanh(c(t)) \tag{10}$$

In equations 5–10, $f(t)$ is the forget gate. σ is the sigmoid function. W_f is the weight in the forget gate controller. X_t is the input at time step t. H_{t-1} is the output at time step t -1. b_f is the bias in the forget gate controller. $i(t)$ is the input gate controller. W_i is the weight in the input gate controller. $b_i$is the bias in the input gate controller. $g(t)$ is the main layer. W_g is the weight in the main layer. b_g is the bias in the main layer. $o(t)$ is the output gate controller. W_o is the weight in the output gate controller. b_o is the bias in the output gate controller. $c(t)$ is the cell state at time t. $h(t)$ is the output.

1.2.6.3 GRU (Gated Recurrent Unit)

Although LSTM avoids the vanishing gradient problem of RNN, LSTM has its drawbacks due to its complex structure requiring relatively high computation power for training. GRU was invented to solve this issue by Junyoung Chung et al. in 2014 [58]. GRU reduces the complexity of the LSTM structure. In GRU, a single gate controller combines the functions of both the forget gate and the input gate. Moreover, the output gate is removed from the structure. Fig. 6 shows a GRU unit cell followed by a list of the equations formulated in the GRU.

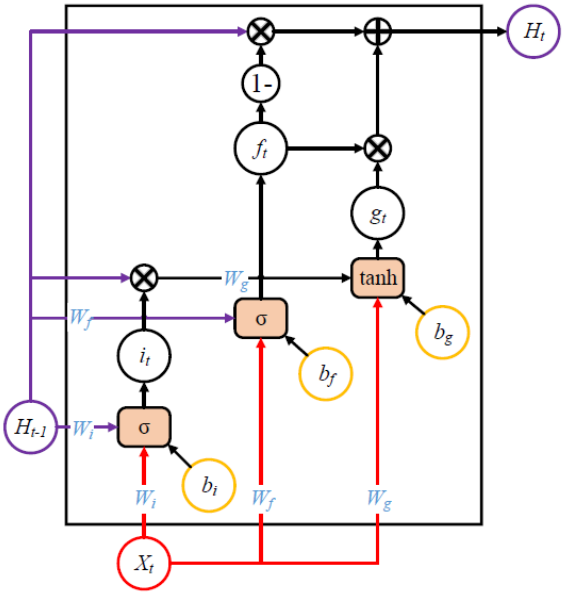

Fig. 6 GRU unit cell [57]

$$f(t) = \sigma\left(W_f X_t + W_f H_{t-1} + b_f\right) \tag{11}$$

$$i(t) = \sigma(W_i X_t + W_i H_{t-1} + b_i) \tag{12}$$

$$g(t) = \tanh\left(W_g X_t + W_g(i_t \otimes H_{t-1}) + b_g\right) \tag{13}$$

$$h(t) = f_t \otimes g_t + (1 - f_t) \otimes H_{t-1} \tag{14}$$

In equations 11–14, $f(t)$ is the single gate controller. σ is the sigmoid function. W_f is the weight in the single gate controller. X_t is the input at time step t. H_{t-1} is the output at time step t -1. b_f is the bias in the single gate controller. $i(t)$ is the new gate controller. W_i is the weight in the new gate controller. $b_i$is the bias in the new gate controller. $g(t)$ is the main layer. W_g is the weight in the main layer. b_g is the bias in the main layer. (Ht) is the output.

1.3 Contributions

The contributions in this dissertation and relevant publications are summarized as follows.

Chapter II assesses two different ANN applications in lithium-ion battery behavior prediction. A comparison study is conducted among various RNN-based lithium-ion battery voltage prediction models in the first application. The comparison work is performed during cold, high c-rate, and long duration profiles. In the second application, an LSTM-based model is proposed to predict the distribution of the battery surface temperatures of a large-sized lithium-ion battery pack.

Gyouho Cho, Di Zhu, and Jeffrey Campbell. A Comparative Study of Recurrent Neural Network Architectures for Battery Voltage Prediction. No. 2021-01-1252. SAE Technical Paper, 2021.

Di Zhu, Jeffrey Campbell, and Gyouho Cho. “Battery Voltage Prediction Using Neural Networks.” 2021 IEEE Transportation Electrification Conference & Expo (ITEC). IEEE, 2021.

Jeffrey Campbell, Di Zhu, and Gyouho Cho. Estimation of Surface Temperature Distributions Across an Array of Lithium-Ion Battery Cells Using a Long Short-Term Memory Neural Network. No. 2022-01-0713. SAE Technical Paper, 2022.

In Chapter III, a PINN method to predict a prismatic lithium-ion battery cell is developed. The proposed PINN model is investigated with the pulse test data. The characteristics of the battery temperature prediction made by the PINN model are reviewed.

Gyouho Cho, Mengqi Wang, Youngki Kim, Jaerock Kwon and Wencong Su, “A Physics-Informed Machine Learning Approach for Estimating Lithium-Ion Battery Temperature,” in IEEE Access, 2022, doi: 10.1109/ACCESS.2022.3199652.

In Chapter IV, the LSTM-PINN hybrid model is developed to predict the distribution of the battery surface temperatures of a large-sized lithium-ion battery pack. This hybrid model improves the temperature prediction by the LSTM model introduced in Chapter II.

Gyouho Cho, Di Zhu, Jeffrey Campbell and Mengqi Wang, "An LSTM-PINN Hybrid Method to Estimate Lithium-Ion Battery Pack Temperature," in IEEE Access, 2022, doi: 10.1109/ACCESS.2022.3208103.

In Chapter V, a comparative study is conducted to assess the effect of various data sampling methods with LSTM architectures for identifying the lithium-ion battery model parameters.

Gyouho Cho, Youngki Kim, Jaerock Kwon, Wencong Su, and Mengqi Wang. “Impact of Data Sampling Methods on the Performance of Data-driven Parameter Identification for Lithium-ion Batteries.” IFAC-PapersOnLine 54.20 (2021): 534–539.

1.4 Dissertation Organization

This dissertation is organized as follows. Chapter II presents the studies proposing RNN methods to predict battery voltage and temperature. Chapter III introduces the PINN for predicting the lithium-ion battery cell temperature during the pulse test. Chapter IV develops an LSTM-PINN hybrid model to predict the distribution of the battery surface temperatures of a large-sized lithium-ion battery pack. This method improves the prediction accuracy of the RNN model introduced in Chapter II. Chapter V discusses the effect of various data sampling methods for battery model parameter identification with the LSTM methods. Finally, Chapter VI summarizes the main results of this dissertation, its contributions, and future research directions.

Chapter 2 RNN For Lithium-Ion Battery Voltage and Temperature Estimation

2.1 Introduction

This chapter presents the RNN applications to predict the lithium-ion battery voltage and temperature. RNN is a sub-category of ANN. In the literature review with the ANN applications for SOC and SOH prediction, the RNN-based methods showed a higher prediction accuracy than other ANN methods because of the RNN's capability to learn the sequential time series data. For lithium-ion battery voltage prediction, a comparison study with three RNN methods, simple RNN, GRU, and LSTM, is made for battery voltage prediction at a low temperature, -30°C, with pulse cycle data. This study uses a 5Ah prismatic lithium-ion battery cell for the pulse test. The LSTM method is proposed to predict the temperature distribution in the lithium-ion battery pack for lithium-ion battery temperature prediction. This development work utilizes battery pack cycle test data with a lithium-ion battery pack consisting of 70 Ah pouch lithium-ion battery cells for the training, validation, and testing of the LSTM model.

This chapter is organized as follows. Section 2.2 contains the comparison study for the lithium-ion battery voltage prediction. Section 2.3 contains the LSTM-based method for the lithium-ion battery temperature prediction. In section 2.3, conclusions are drawn.

2.2 RNN Methods to Predict Battery Voltage

This section contains a comparative study with three RNN methods, simple RNN, GRU, and LSTM, for predicting lithium-ion battery cell voltage at a low temperature, -30°C. In the comparison study, multiple pulses profiles with different pulse sizes and a rest between the two pulses are applied to the three neural network structures to assess the prediction accuracy for both dynamic and relaxation lithium-ion battery behaviors. After reviewing the prediction accuracy, this section of the dissertation will propose the most suitable RNN structure for lithium-ion battery voltage prediction.

2.2.1 Sliding Window and Many-to-One Architectures

In this comparison study, the sliding window and many-to-one architectures combine with each RNN structure to predict the lithium-ion battery cell voltage from the previous sequence information. In the sliding window approach, the previous 20 sequences in the time series data are fed to each RNN type to predict a current battery cell voltage. Also, this approach uses multiple inputs, current, voltage, and SOC, which categorize this method as a many-to-one architecture. The schematic input and output data flows are described in Fig. 7.

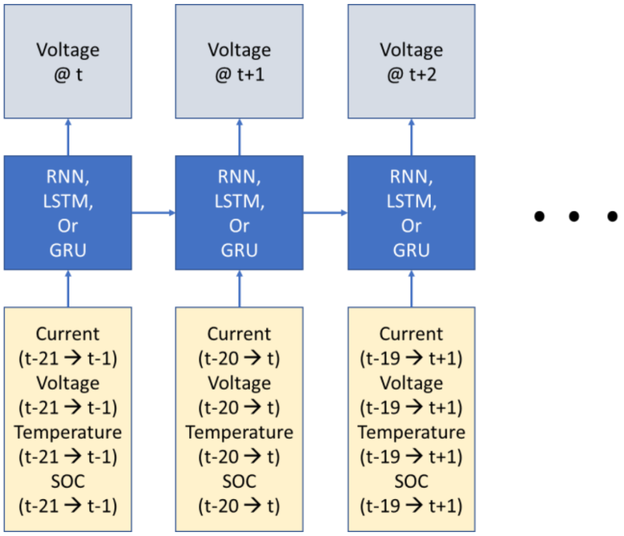

Fig. 7 Sliding window and many-to-one architecture

2.2.2 Data Acquisition and Preparation—Voltage Prediction

Current-pulse tests are conducted to prepare the training data for the three RNNs. This pulse test contains 10-seconds-long constant current pulses with different current sizes, the rest time between the two different pulses, and small current pulses to maintain the state of charge during the test. With this profile, the three RNNs are under evaluation during both large current sizes and relaxation. Furthermore, to conduct the comparative study at low temperature, the current pulse test is performed at 25°C and -35°C. However, since a lithium-ion battery has a high resistance that causes the early end of the test to reach the battery voltage limit during the test, the size of the current pulses in the -35°C pulse test profile is smaller than those of the 25°C pulse test profile. For the 25°C pulse test profile, 10-second discharge pulses from 20A to 200A with a 20A increment change are applied. For the -35°C pulse test profile, 10-second discharge pulses from 2A to 16A with a 2A increment change are applied. In Fig. 15, the current profiles of the pulse tests at 25°C and -35°C are provided.

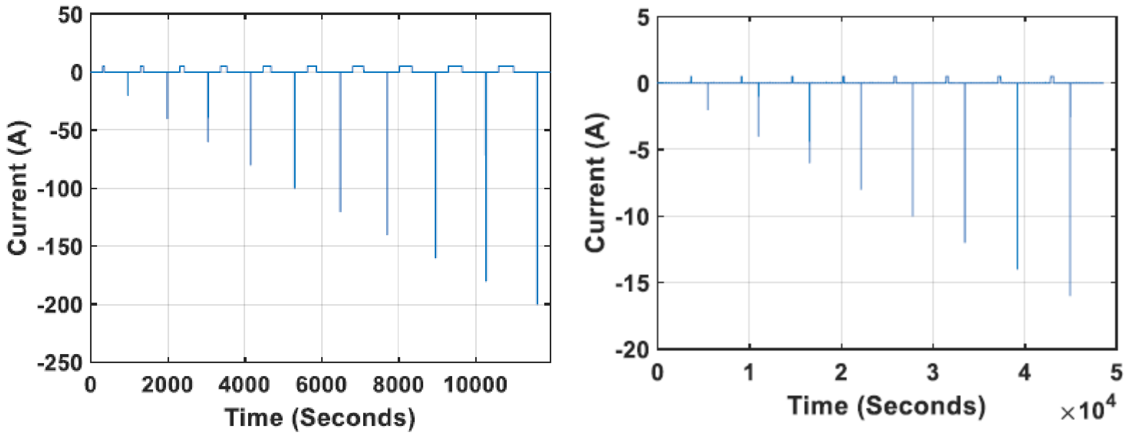

Fig. 8 Pulse test profile at 25°C (left) and -35°C (right), (negative: discharge)

In the current pulse test, a 5Ah prismatic lithium-ion cell is used as a test sample. An Arbin battery cycler and AVL battery tester are connected to the test sample in the test setup. The test sample is secured inside the environmental chamber to control the test temperature. Prior to the beginning of the test, the battery sample is set to the desired SOC and thoroughly soaked to the test temperature. The detailed test sample information and a schematic view of the test setup are provided in Table 8 and Fig. 9.

Table 7 Lithium-ion battery test sample information

	Specification
Capacity (Ah)	5
Format	Prismatic
Cathode Chemistry	NMC
Anode Chemistry	Graphite
Dimension (mm)	12.5 (T) x 120(W) x 70(H)

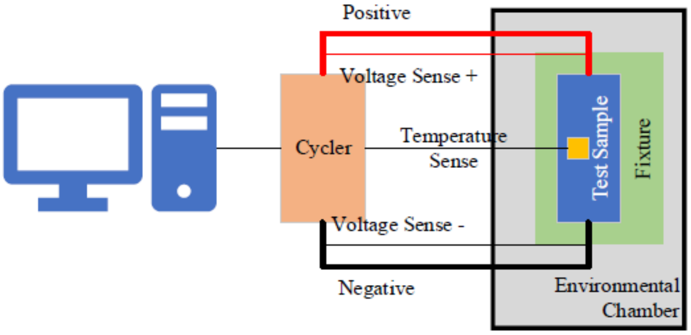

Fig. 9 Battery pulse test setup

Table 8 SOC and temperature conditions in the pulse test

Temperature (°C)	SOC (%)
25	40
25	50
25	60
-30	40
-30	50
-30	60

The temperature and SOC test conditions for the lithium-ion battery cell test are given in Table 8. SOC test conditions are selected based on the working SOC window of the battery sample in the hybrid vehicle application. The SOC test conditions are chosen as the highest, lowest, and middle SOC levels in the working SOC window. In the test, the battery cell voltage between the battery terminal, SOC, battery temperature, and current are recorded at the sampling rate of 1 second. The Ah throughput is calculated based on the current measurement for the SOC measurement. Then it is divided by the discharge capacity pre-determined before the pulse test. For the temperature measurement, the thermocouple is located on the surface of the middle part of the battery cell. After the data acquisition, all measurement data are normalized between -1 and 1 because the hyperbolic tangent function used in the RNNs as the activation function ranges between -1 and 1. The normalization formula is given in the equation below.

$$x_{new} = \frac{x_{original} - x_{mid}}{x_{\max} - x_{mid}} \tag{15}$$

In the equation, x_{new} is the measured data after the conversion, $x_{original}$ is the measured data, x_{mid} is the median value of the measured data, and x_{max} is the maximum value of the measured data. The ranges of the measured data and the median values are provided in Table 9.

Table 9 Range and median of the measured data

	Maximum	Median	Minimum
Voltage (V)	4.2	3	1.8
SOC (%)	100	50	0
Current (A)	300	0	-300

In the prediction model with the trained RNNs, the outcome from the RNN is inversely normalized to find the battery voltage.

2.2.3 Training Process—Voltage Prediction

The same training data sets are applied for the RNN, GRU, and LSTM to ensure that the three RNNs are trained with the same data. For the training, 70% of the measured data is allocated for the training process, 20% of the measured data is allocated for the validation process, and 10% is allocated for testing the trained RNNs to evaluate the prediction accuracy. Table 10 shows the hyperparameters applied to the training process.

Table 10 Hyperparameters applied during the training process

Hyperparameter	Value
Batch size	200
Sliding window size	20
Epochs	50
Dropout Rate	1%

2.2.4 Results—Voltage Prediction

The 10% of the measured data allocated to evaluate the three RNNs is the high pulse discharge event with the four discharge pulses, the three charge pulses for the SOC adjustment to maintain the SOC level, and the rest time between the pulses. This event takes place at -30°C and SOC 50%. Fig. 10 shows the measured and predicted voltages by the simple RNN method in the test process in which the prediction error is evaluated. Also, since there are multiple pulses in the evaluation process with the prediction behaviors from the three RNNs, the last charge and discharge pulses with the highest pulses are selected to represent the critical features in the predictions. Fig. 11 provides the charge pulse with the measured and predicted voltages by the three RNNs. Fig. 12 provides the discharge pulse with the measured voltage and the predicted voltages by the three RNNs.

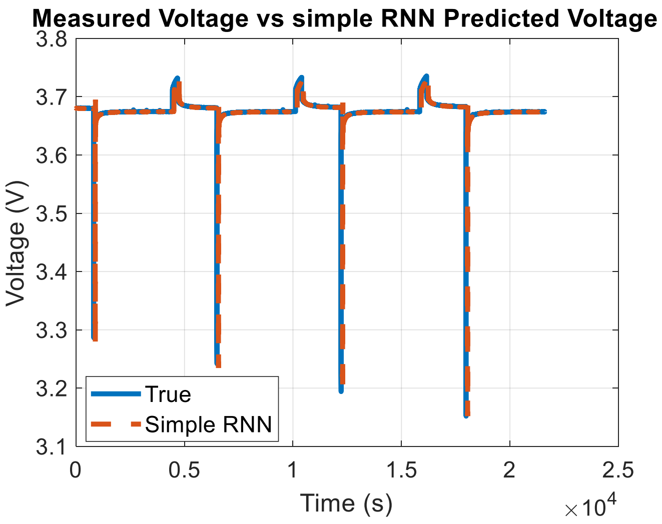

Fig. 10 Battery pulse test setup at -30°C

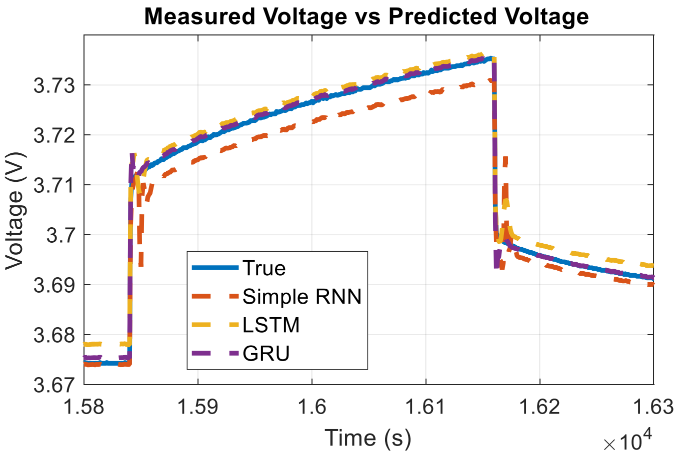

Fig. 11 Measured voltage vs predicted voltage in the charge pulse for all RNNs at -30°C

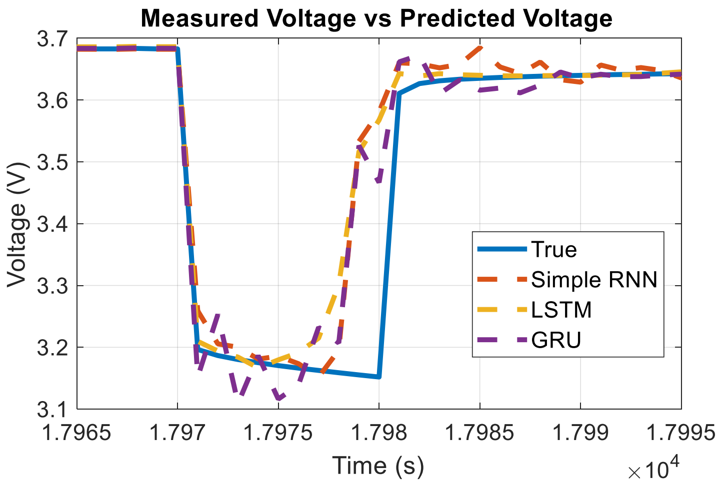

Fig. 12 Measured voltage vs predicted voltage in the discharge pulse for all RNNs at -30°C

Lastly, the root mean square error (RMSE) and mean absolute error (Max AE) of the three RNN cases during the test process are computed for the comparative study. Table 11 has the RMSE and Max AE of all three RNNs at -30°C and 25°C.

Table 11 RMSE of RNN, GRU and LSTM using test data set at -30°C and 25°C

Temperature (°C)	**RNN models**	**RMSE (V)**	**Max AE (V)**
-30	Simple RNN	6.95E-03	0.53
	GRU	6.14E-03	0.55
	LSTM	7.81E-03	0.53
25	Simple RNN	1.20E-02	0.37
	GRU	1.22E-02	0.22
	LSTM	8.92E-03	0.41

2.2.5 Discussion—Voltage Prediction

As indicated in Fig. 11, the prediction made by the simple RNN method has a late voltage prediction convergence speed with a significant prediction error during the charge pulse at -30°C. LSTM and GRU methods have a fast convergence speed, but the LSTM method has a more significant prediction error during the relaxation time than the GRU method. For the voltage prediction during the discharge pulse, as shown in Figure 12, the LSTM method has the fastest prediction convergence speed compared with the other two RNNs. In the case of the prediction made by the simple RNN, the voltage prediction begins to lag the measured voltage at the end of the pulse. Overall, the voltage prediction made by LSTM is close to the measured voltage, with smooth curvature.

Furthermore, the voltage prediction by the LSTM method is robust against temperature and pulse size. In Table 12, the RMSEs of the voltage predictions by the simple RNN and GRU methods increase in 25°C, in which the pulse size is also more prominent compared with that at the low temperature. At -30°C, the pulse size is limited due to the high battery resistance to avoid hitting the operation voltage limit during the battery test. For both temperature conditions, only the voltage prediction made by the LSTM method maintains the same order of magnitude in the prediction error. This prediction accuracy at both temperatures demonstrates that the LSTM unit structure that is designed to avoid the gradient vanish or explode problem also effectively manages sudden current and voltage changes in the input signals.

For voltage prediction in the low temperature at -30°C, the LSTM method has the same magnitude of prediction error as in the moderate temperature at 25°C. This prediction behavior indicates that the temperature has a limited influence on the voltage prediction error for the LSTM method. Indeed, this robust prediction error behavior against temperature is expected because, during the training process, the LSTM method learned the lithium-ion battery cell voltage behavior at the low temperature from the battery test data. This learning from the data is a strength of the data-driven battery model since it does not require any characterization process to predict the battery voltage at a low temperature. For other battery voltage estimation methods, such as the lithium-ion battery model-based method, the electrochemical and thermal properties of the lithium-ion battery are necessary to predict the battery voltage.

In summary, the LSTM method has a higher prediction accuracy, faster convergence, and robustness against the external temperature than the simple RNN and GRU methods to make the lithium-ion battery voltage prediction. In the literature review, the RNN methodology shows the best prediction accuracy among other ANN methods for lithium-ion battery parameters estimations, such as SOC and SOH estimations, due to its capability to learn the sequential data. Therefore, it is also safe to claim that the LSTM method, which is a kind of RNN method, offers the most accurate prediction for lithium-ion battery behavior such as the battery voltage among the ANN methods.

2.3 LSTM Method to Predict Battery Temperature

Lithium-ion battery temperature is another significant form of the battery response influencing the battery performance, safety, and life. This section of the dissertation paper proposes an LSTM method to predict the lithium-ion battery temperature at various locations in a high-energy lithium-ion battery pack. Like the RNN architecture reviewed in the previous section, the LSTM method discussed in this section is also based solely on the battery test data to learn the lithium-ion battery thermal behavior.

2.3.1 Method

For the LSTM method, the inputs are the two-reference battery temperatures in the battery pack, battery voltage, battery current, SOC, and ambient temperature. The output of the LSTM method is the battery temperatures at three different locations in the battery pack. The locations of the input and output temperatures inside the lithium-ion battery pack are given in the layout provided in Fig. 13. Also, the battery temperature prediction process of the LSTM method is shown in Fig. 14.

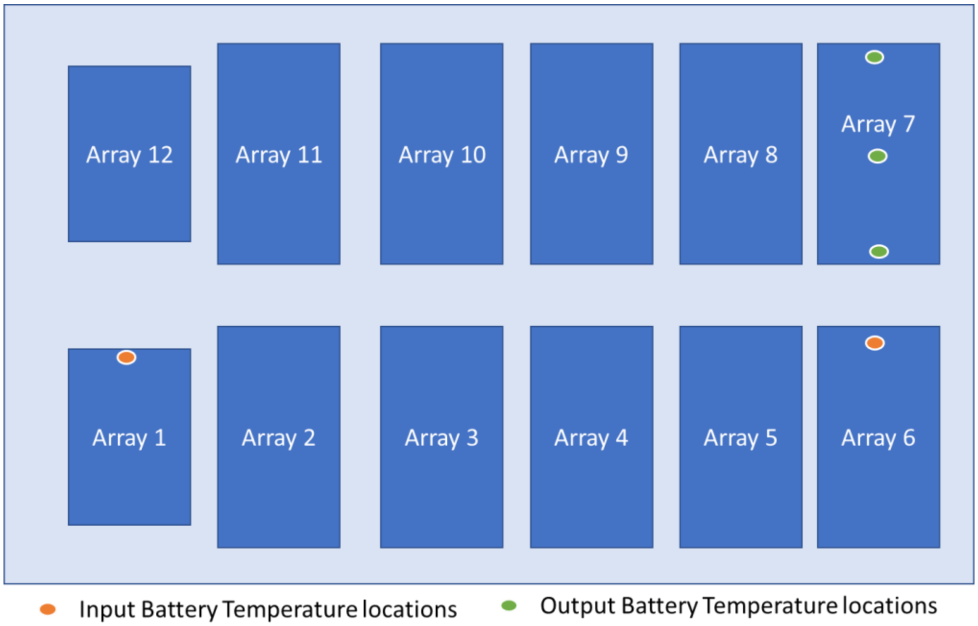

Fig. 13 Input and output temperature locations in the lithium-ion battery pack (Array represents a group of the lithium-ion battery cells in the battery pack) [59]

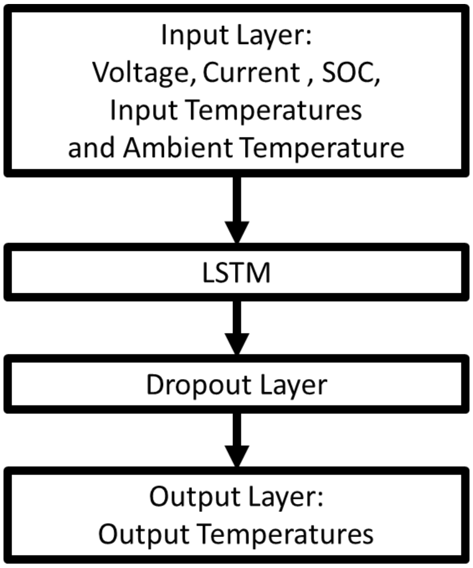

Fig. 14 LSTM method process [59]

2.3.2 Data Acquisition and Preparation—Temperature Prediction

This study conducts battery cycle tests to generate the test data for the LSTM method training, validation, and testing. Table 12 lists the test equipment used in the battery test, and Fig. 15 shows an overview of the test setup implemented during the battery test.

Table 12 List of the test equipment [59]

#	Equipment	#	Equipment
1	Thermotron thermal chamber	4	Omega T-type thermocouples
2	AV-900 EX cycler	5	Gantner DAQ
3	Polyscience coolant chiller	6	PC with AVL software

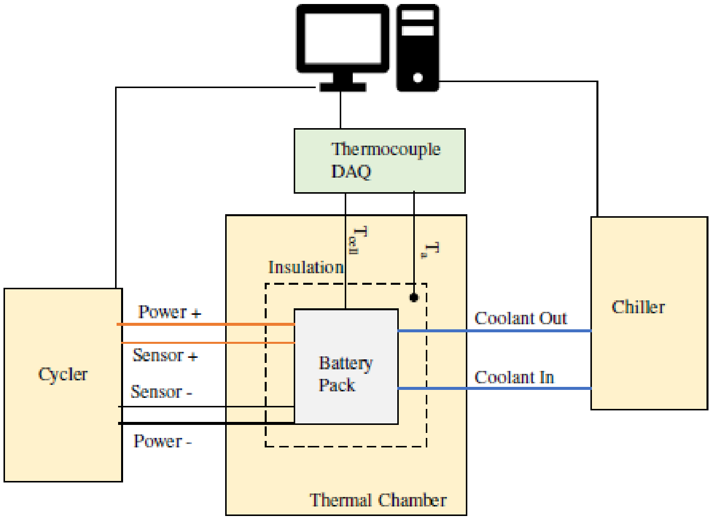

Fig. 15 Overview of the battery pack test setup

This battery pack test uses a battery pack consisting of 464 lithium-ion battery cells. 40 cells are electrically connected in the battery arrays except for battery arrays #1 and #12 in Fig. 13. For battery arrays #1 and #12, each of them has 32 lithium-ion battery cells. The specifications of the lithium-ion battery cell are provided in Table 13.

Table 13 Lithium-ion battery cell specifications [59]

	Specification
Capacity (Ah)	70
Type	Pouch
Cathode Chemistry	NMC (nickel manganese cobalt)
Anode Chemistry	Graphite
Dimension	14(T) × 300(W) × 100(H)

For the thermocouple placement, the input temperature readings are done at the end of array #1 and array #6 described in Fig. 13. These two spots are selected because of the minimum temperature by the heat sink near array #1 and the proximity to array #7 in which the output temperature measurements are carried out. A total of three output measurements are recorded in array #7: two end cells and one middle cell.

For the battery pack cycle test, various drive profiles are applied to the battery pack with a data sampling rate of 1Hz. Table 14 includes all the drive profiles. In Table 14, the initial temperature indicates the minimum battery cell temperature after soaking the battery pack to the chamber setpoint. Coolant temperature is the control temperature of the chiller during the pack test. All drive profiles used in this study are provided in the Appendix of this dissertation paper.

Table 14 Drive profiles and test conditions used in the battery test [59]

Drive Profile	Initial Temperature (°C)	Coolant Temperature (°C)	Usage
MCT	30	15	Training
Vmax	38	15	Training
US06	20	20	Training
FTP20	-7	15	Training
DCFC	30	15	Training
DCFC	-7	15	Validation
DCFC	40	15	Test
GL100	38	15	Test

2.3.3 Training Process—Temperature Prediction

Before training the LSTM with the input data, normalization of the input data takes place to scale the input data between 0 and 1. This process is formulated in equation (16).

$$x_{new} = \frac{x_{original} - x_{min}}{x_{\max} - x_{min}} \tag{16}$$

In (15), x' represents the scaled input variable, x is the input variable, x_{min} is the minimum value expected for the input variable, and x_{max} is the maximum expected value for the input variable. x_{min} and x_{max} are selected from the operating conditions of the lithium-ion battery cell. The maximums and minimums of the input variables are listed in Table 15.

Table 15 Maximum and minimum of the input variables [59]

	Voltage (V)	SOC (%)	Current (A)	Temperature (°C)
Maximum	425	100	400	60
Minimum	250	0	-400	-30

After the normalization of the input data, the training, validation, and testing of the LSTM method are performed. Drive profiles used in this study are allocated to the training, validation, and test processes as in Table 14. It is noted that the test data are not provided to the LSTM method before the final performance evaluation to avoid a biased evaluation of the LSTM method [60].

For the hyperparameter optimization, sets of hyperparameters designed by the design of experiments method are applied to the multiple runs of the training, validation, and test processes. The optimum hyperparameter is selected from the hyperparameters producing the highest prediction accuracy. These optimum hyperparameters are applied to the battery temperature prediction study. The hyperparameters used in this study are provided in Table 16.

Table 16 Hyperparameters used in the battery temperature prediction

Hyperparameter	Value
Batch Size	60
Lookback	1
Epoch	100
Dropout Rate	3%

2.3.4 Results—Temperature Prediction

The DCFC profile at 40 °C and the GL100 profile at 38 °C are assigned to test the LSTM method to predict the battery temperatures at the three locations in array #7 of the battery pack. Fig. 16 and Fig. 18 include the true and prediction temperatures for the DCFC and GL100 profiles.

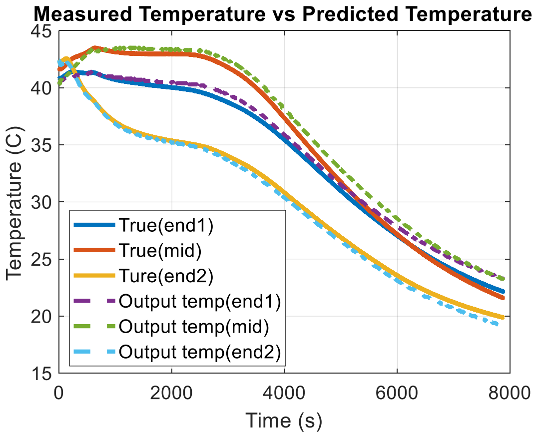

Fig. 16 Measured vs. predicted temperatures during the DCFC profile at 40°C ambient.

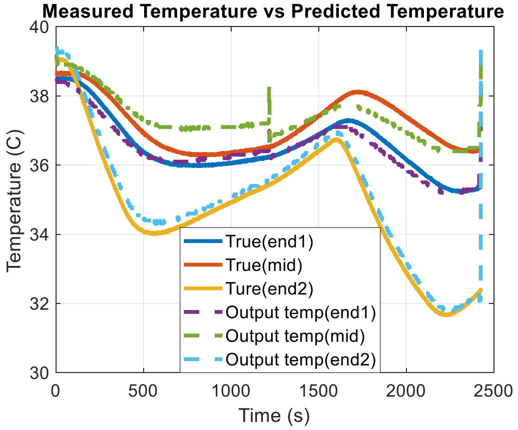

Fig. 17 Measured vs. predicted temperatures during the GL100 profile.

Lastly, the RMS of the three output temperatures during the DCFC and GL100 profiles are computed. Table 17 has the RMS of all cases.

Table 17 RMS of the three output temperatures during the DCFC and GL100 profiles

(°C)	DCFC	GL100
Output temp (end 1)	0.64	0.22
Output temp (middle)	1.01	0.48
Output temp (end 2)	0.40	0.32

2.3.5 Discussion—Temperature Prediction

The results of the tests show that the LSTM method can predict the battery pack temperature with a prediction accuracy of 1°C or better. Also, the RMS analysis shows that most of the prediction errors are less than or near 0.5°C, which is the measurement tolerance of the thermocouple. This level of prediction error indicates that the LSTM method is suitable for modeling the thermal behavior of the large-scale lithium-ion battery pack without identifying the thermal properties of the battery, such as thermal capacity and thermal transfer coefficients.

However, there is a shortcoming with the LSTM method. From Table 17, it is observable that the RMS error of the middle temperature is larger than that of the other two temperatures located at the edges of battery array #7. For the test results of the DCFC profile, the RMS error of the middle temperature is around 1°C, which is greater than the other test results. For the GL100 profile, although the RMS error is less than that for the DCFC profile, the RMS error of the middle temperature is also greater than the two temperature prediction results at the ends of battery array #7. This RMS error pattern is because the inputs to the LSTM method contain the temperatures at only the ends of battery arrays #1 and #6. The temperature predictions at the middle of battery #7 rely on the interpolation capability of the LSTM method, which has learned the thermal behavior of the battery pack based on the test data containing the temperature information only at the edges of the battery array. Therefore, insufficient training data regarding the temperature at the geometry not presented in the training data causes the inaccuracy of the temperature prediction by the LSTM method.

2.4 Conclusion

In this chapter, RNN methods are developed to predict the lithium-ion battery voltage and temperature. A comparative study with the three different RNN methods is conducted for the battery voltage prediction. From the outcome of this study, the LSTM method is selected as the most suitable RNN method to predict lithium-ion battery voltage due to its high prediction accuracy, fast convergence, and robustness against external temperature such as -30°C. With the characteristic of the data-driven method, the LSTM method also does not require any battery characterization information to make the prediction. In the second half of the chapter, the LSTM method has been applied to predict the battery temperature at various locations in the large-scale battery pack. This study also demonstrates that the LSTM method could predict the temperature with a low prediction error of less than 1°C while cycling the drive profiles. This temperature prediction by the LSTM method is also made without information on the thermal characteristics of the lithium-ion battery.

However, the temperature prediction case study shows the LSTM method's shortcoming, which is learning the battery thermal behavior based solely on the battery test data. In the study, the temperature prediction at the location not presented in the training data has less accurate prediction accuracy. This observation shows the significance of the data for the LSTM method, and it is also the disadvantage of the LSTM method when it learns only from the collected data. To improve this shortcoming, the next chapter of this dissertation paper will introduce the physics-informed neural network (PINN) method to diversify the sources for the learning process.

Chapter 3 PINN for Lithium-ion Battery Cell Temperature Estimation

3.1 Introduction

As presented in Chapter 2, an ANN method, such as the LSTM method, has the benefits of predicting lithium-ion battery behavior without any battery characterization information. Also, it has high prediction accuracy in lithium-ion battery applications, which conventionally require high computation or intensive system identification, such as the low-temperature voltage behavior and large-scale battery pack temperature estimations. However, the LSTM method based solely on the data cannot predict what is not sufficiently contained in the training data. This dissertation proposes the physics-informed neural network (PINN) to improve this limitation of the data-driven method, in which both data and physics laws are applied together to train the neural network. In this chapter, the lithium-ion battery cell temperature during the pulse battery test is estimated by PINN. This study uses a 5Ah prismatic lithium-ion battery cell.

This chapter is organized as follows. Section 3.2 presents background information on the PINN. Section 3.3 elaborates on the methodology to create the lithium-ion battery cell data and to train the PINN method. Section 3.4 contains a comparative study to evaluate the benefits of the PINN method over the ANN method. Section 3.5 contains another comparative study to obtain the optimum pre-layer architecture of the PINN method. Lastly, section 3.6 presents the conclusion of the PINN study in this chapter.

3.2 Physics-Informed Neural Network (PINN)

As the battery temperature study in the previous chapter indicated, the ANN methods depend solely on the data and have the drawback of low prediction accuracy when local data scarcity occurs. The lack of training data forces the ANN methods to predict without adequate learning. PINN is a method that can strengthen the ANN method to overcome this shortcoming. PINN utilizes both physics laws and data to train neural networks. These characteristics of the PINN enable it to capture the benefits of a conventional data-driven method such as the ANN and the model-based method, which relies on physics laws to estimate. Table 18 compares the three prediction methods: model-based, data-driven (e.g., ANN), and PINN.

Table 18 Model-based method vs. Data-driven method vs. PINN method [61]–[63]

		Prediction Method		
		Model-Based	**Data-Driven**	**PINN**
Characteristic	**Physics Laws Implementation**	Highly depends on physics	No physics laws	Some physics laws
	Data Requirement	Small data	Big data	Some data
	Model Identification	Required	-	Not identified models acceptable (model identification made during the training process)
	Imperfect Data	Impact on the model identification	Not well-trained method	Robust to the imperfect data

With its characteristics combining data and physics models, many pieces of literature proposed the PINN to solve engineering challenges. The PINN method has applications in fluid dynamics [64]–[68], solid mechanics [69]–[71], optics [72]–[74], metallurgy [75], heat transfer [76]–[79], and earth system science [80]. In all PINN examples, the literature implements the physics equations and data from either tests or simulations to make successful predictions. Furthermore, PINN could be applied to the ANN using published software such as DeepXDE

[81], NVIDIA SimNet™ [82], SciANN [83], Elvet [84], TensorDiffEq [85], PyDEns [86], NeuroDiffEq [87], and NeuralPDE [88]. In this research project, the PINN is implemented by the customized script developed by TensorFlow.

For the implementation of the PINN method, three main approaches could be applied to the ANN methods. First, the loss function of the ANN is altered to include the physics laws, initial condition, and boundary condition [63]. Second, the adaptive coefficients are utilized for the loss function. Third, the neural network topology is constructed to reflect the solution of the physics model. The following three subsections will discuss the details of the three approaches.

3.2.1 Loss Function with Physics Information

Loss function modification is the most popular way to construct the PINN method in the literature [61]–[63]. In this methodology, multiple loss functions are defined. The first loss function minimizes the residuals between the predictions and true values. Usually, mean square error calculation is implemented in the first loss function as other regression ANN methods use only the data. The formulation of this loss function is provided in (17).

$$Loss_r = \frac{1}{N}\sum_{i=1}^{N}\left|Y_{pre}^{i} - Y_i\right|^2 \tag{17}$$

In (16), N is the number of training data, Y_{pre}^{i} is the prediction value, and Y_i is the true value. The estimation error occurred from the physics law or model for the second loss function. The formulation of this loss function is provided in (18).

$$Loss_f = \frac{1}{N}\sum_{i=1}^{N}|f|^2 \tag{18}$$

In (18), N is the number of training data, and f is the value calculated from the physics law or model. If the given physics law is ideally identified without any error, $Loss_f$ should equal zero. The third loss function is related to the physics law's initial and boundary conditions. In (19) and (20), the loss functions are formulated for the initial and boundary conditions.

$$Loss_{initial} = |f(t = 0) - Y_{ini}|^2 \tag{19}$$

$$Loss_{boundary} = \left|f\left(x_{boundary}\right) - Y_{boundary}\right|^2 \tag{20}$$

In (18), $f(t = 0)$ is the value of the physics law at the initial condition, and Y_{ini} is the actual initial value. In (19), $f\left(x_{boundary}\right)$ is the value of the physics law at the boundary condition. $Y_{boundary}$ is the actual boundary value. In sum, the overall loss function in the PINN is formulated as (21).

$$Loss_{total} = Loss_r + \alpha Loss_f + \beta Loss_{initial} + \gamma Loss_{boundary} \tag{21}$$

In (20), α, β, and γ are the adaptive and normalized coefficients, which will be discussed in the next section.

3.2.2 Adaptive Normalization Factor in Loss Function

As presented in the previous section, the loss function of the PINN method has multi-loss terms. In the literature, several methods exist to identify each term's coefficient in the loss function. In [89], the non-adaptive coefficient in the loss term has been applied to the PINN method with a much larger coefficient for the initial condition-related loss term. In [76] and [90], the proposed methods adjust the coefficients in the loss function based on the learning rate without backpropagation. In [91], the neural tangent kernel matrix is used to find the adaptive coefficients in the loss function. In [92], gradient ascent is applied to estimate the coefficients. Finally, in [93], a soft attention mechanism is proposed to set the coefficients in the loss function. In the research work presented in this dissertation paper, the learning rate annealing algorithm is implemented as proposed in [90]. This learning rate annealing method has a successful history in the literature in making a temperature prediction with a heat transfer model, which is like the battery thermal model.

The learning rate annealing algorithm has two steps to identify the coefficients in the loss function. In the first step, the learning rate annealing method computes the ratios between the maximum backpropagation gradient of the residual loss term and the mean backpropagation gradient of the other loss terms. Then the instant scaling factors are defined for the physics model, initial condition, and boundary condition. Instant scaling factors $\hat{\alpha}$, $\hat{\beta}$, and $\hat{\gamma}$ are formulated as (22)–(24).

$$\hat{\alpha} = \frac{max\,\{|\nabla Loss_r|\}}{|\overline{\nabla Loss_f}|} \tag{22}$$

$$\hat{\beta} = \frac{max\,\{|\nabla Loss_r|\}}{|\overline{\nabla Loss_{\iota n\iota t\iota al}}|} \tag{23}$$

$$\hat{\gamma} = \frac{max\,\{|\nabla Loss_r|\}}{|\overline{\nabla Loss_{boundary}}|} \tag{24}$$

In the second step, the coefficients of the loss function are computed from the moving average between the coefficients and the instant scaling factors from the previous epoch. The mathematical formula for this step is provided in (25)–(27).

$$\alpha = (1-\delta)\alpha_{previous} + \delta\hat{\alpha}_{previous} \tag{25}$$

$$\beta = (1-\delta)\beta_{previous} + \delta\hat{\beta}_{previous} \tag{26}$$

$$\gamma = (1-\delta)\gamma_{previous} + \delta\hat{\gamma}_{previous} \tag{27}$$

In (25)–(27), α, β, and γ are the adaptive and normalized coefficients in the loss function. $\alpha_{previous}$, $\beta_{previous}$, and $\gamma_{previous}$ are the adaptive and normalized coefficients in the loss function in the previous epoch. $\hat{\alpha}_{previous}$, $\hat{\beta}_{previous}$, and $\hat{\gamma}_{previous}$ are the instant scaling factors in the previous epoch. δ is a tunable hyperparameter.

3.2.3 PINN Architecture

A neural network architecture in the PINN method is another area that could be designed to promote biased learning to implement the physics laws in the PINN method. In [76], the author proposed the pre-layer and connection layer, either a concatenate or a multiply layer, for the neural network architecture to enhance the prediction accuracy of the PINN method. This architecture was derived from the analytical solution of the thermal model equation, which was the physical law implemented in the PINN method.

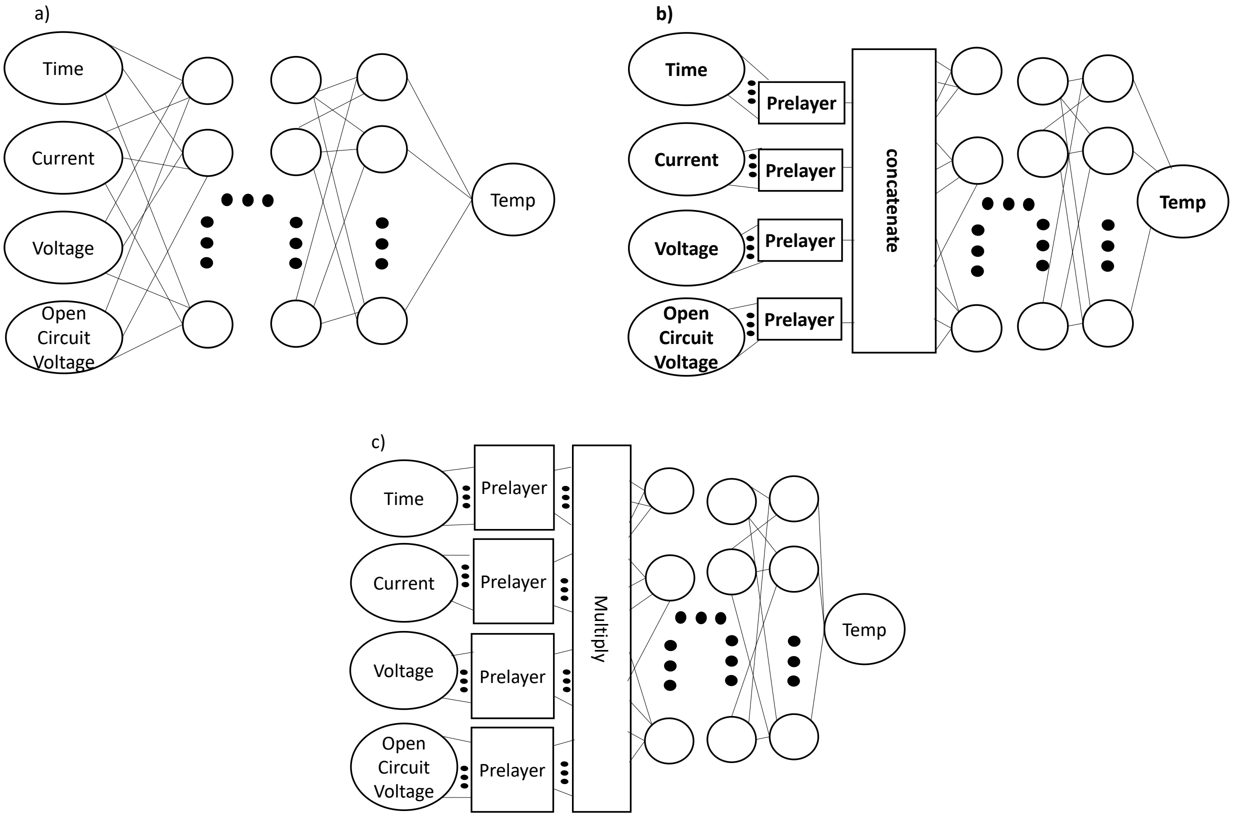

Fig. 18 Three PINN architectures in the comparative work: (a) ANN structure, (b) ANN structure with the pre-layer and concatenate layer and (c) ANN structure with the pre-layer and multiply layer

In the research work presented in this chapter, a comparative study will be conducted to develop the most suitable neural network architecture for predicting the lithium-ion battery cell temperature. The ANN structure proposed in [76] will be reinvented to predict the lithium-ion battery cell temperature. In the comparative work, the ANN structure, the ANN structure with the pre-layer and concatenate layer, and the ANN structure with the pre-layer and multiply layer will be evaluated. Fig. 18 shows the three architectures in the comparative work.

3.2.4 PINN vs. ANN

The three approaches applied to the PINN integrate the battery thermal model and battery test data. During the training, the loss function containing both residual loss and other loss terms associated with the battery thermal model and boundary conditions induces the bias learning so that the prediction made by the PINN minimizes the difference between the true and predicted values while the thermal model and boundary conditions are applied to the prediction. The ANN method excludes the thermal model and boundary conditions from the ANN's learning process. The loss function of the ANN only contains the residual loss term; therefore, the ANN only learns from the battery test data to minimize the difference between the true and predicted values. Table. 19 presents the difference between PINN and ANN based on this study's three approaches to building the PINN.

Table 19 PINN vs. ANN

		PINN	ANN
Characteristic	Loss function	$Loss_{total} = Loss_r + \alpha Loss_f + \beta Loss_{initial} + \gamma Loss_{boundary}$	$\text{Loss} = Loss_r$
	Adaptive Normalization in the loss function	Benefits to enhance the prediction accuracy	Not required
	Architecture	Considering the analytical solution of the physics law	No effect from the physics law

3.3 Method

3.3.1 Battery Thermal Model

For the lithium-ion battery temperature prediction, the PINN method proposed in this chapter implements the lumped capacitance thermal model as the physics law with the assumption that the temperature distribution in the lithium-ion battery is uniform. The lumped capacitance thermal model is formulated as (28).

$$mC_p\frac{dT}{dt} = \dot{Q} + hA(T_{amb} - T) \tag{28}$$

In (27), m is the mass of the lithium-ion battery, C_p is the heat capacity of the lithium-ion battery, T is the lithium-ion battery temperature, t is time, $\dot{Q}$ is the heat generation during the battery operation, h is the convectional heat coefficient, and T_{amb} is the ambient temperature inside the climate chamber. For the heat generation in (28), this study considers only the irreversible heating of the lithium-ion battery since it is the largest source of heat generation. Any other heat generation effects not considered in the study are not expected to influence the temperature prediction outcome because the PINN method is robust against the incompleteness in the physics model. The irreversible heat generation is formulated as (29).

$$\dot{Q} = (V - V_{ocv})I \tag{29}$$

In (28), V is the battery voltage, V_{ocv} is the open-circuit battery voltage, and I is the current applied to the battery during the battery test. To apply the lumped capacitance thermal model to the PINN method, (28) and (29) are combined and rearranged as (30).

$$f = \frac{dT}{dt} + \lambda_1(V - V_{ocv})I + \lambda_2(T_{amb} - T) = 0 \tag{30}$$

In (29), f is the physics model applied to the PINN, and λ_1 and λ_2 are the coefficients of the thermal equation. Two coefficients will be identified during the training process using the L-BFGS-B method.

With this lithium-ion battery thermal model, the loss function of the PINN method is updated as follows. The regression loss function term is formulated as (31).

$$Loss_r = \frac{1}{N}\sum_{i=1}^{N}\left|T_{pre}^{i} - T_i\right|^2 \tag{31}$$

In (31), N is the number of training data, T_{pre}^{i} is the temperature predicted by the neural network, and T_i is the true temperature. For the loss term related to the physics law, the loss term is formulated as (32).

$$Loss_f = \frac{1}{N}\sum_{i=1}^{N}|f|^2 \tag{32}$$

In (32), f is given in 29. Also, the loss term related to the initial condition is formulated in (33). There is no loss term related to the boundary condition.

$$Loss_{initial} = |f(t = 0) - T_{amb}|^2 \tag{33}$$

3.3.2 Lithium-Ion Battery Cell Test

This research project conducted battery cell tests to obtain the data for training and testing the PINN method. The battery cell test data included battery voltage, battery current, battery temperature, and chamber temperature. Additionally, the input data included the open-circuit voltage (OCV), estimated by the OCV and SOC table created by the lithium-ion battery manufacturer. The SOC of the lithium-ion battery was calculated by the Ah-integration method.

In the battery test, a prismatic lithium-ion battery cell was cycled with 5A charge and discharge pulses and 20 minutes rest between the charge and discharge pulses. The specifications of the lithium-ion battery cell are provided in Table 19. Moreover, Fig. 19 shows the current profile applied to the battery test.

Table 20 Lithium-ion battery cell specifications

	Specification
Capacity (Ah)	5
Format	Prismatic
Cathode chemistry	NMC
Anode chemistry	Graphite
Dimensions (mm)	120(W)× 12.5(T)×70(H)

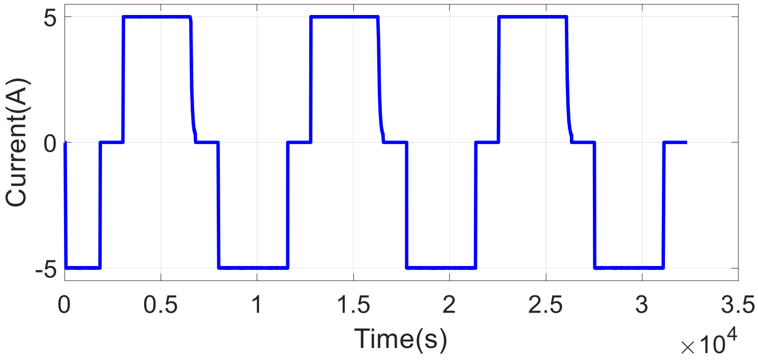

Fig. 19 Charge and discharge battery cycle profile

The battery cell test sample was placed in a climate chamber during the lithium-ion battery cell test. Also, the battery cell test sample was connected to the battery cycler and data acquisition system via thermocouples, voltage sensors, and power lines, as illustrated in Fig. 20.

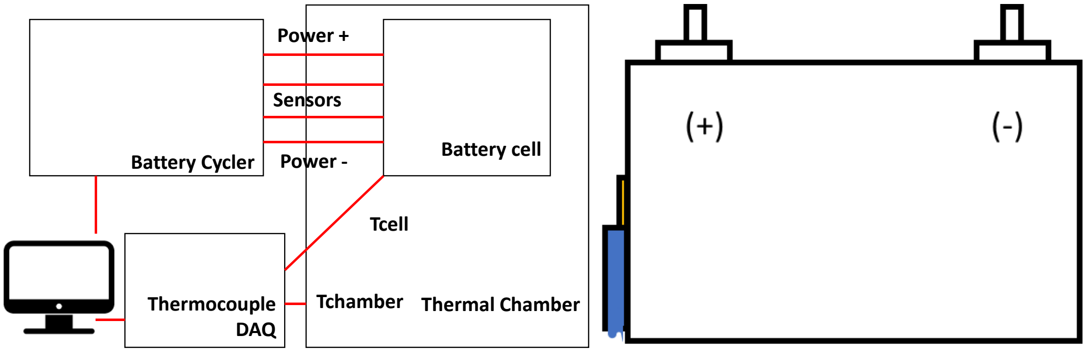

Fig. 20 Battery test setup overview (left); thermocouple setup on the battery cell (right)

3.3.3 Training Process

For the training of the PINN method, this study uses the first 35% of the lithium-ion battery cell data. The training data size is purposely limited to cause training data scarcity. After collecting the lithium-ion battery cell data, preprocessing of the test data is conducted to normalize the test data. (34) contains the normalization formula implemented in this study.

$$\acute{x} = \frac{x - x_{min}}{x_{max} - x_{min}} \quad (34)$$

In (33), $\acute{x}$ is the normalized test data, x is the test data, x_{min} is the minimum of the test data, and x_{max} is the maximum of the test data. After the test data normalization, the training of the PINN method is conducted. In training, a set of hyperparameters is applied to the PINN method. The hyperparameters are tuned based on other hyperparameter tunings with a similar thermal application in the PINN literature or from the tests planned with the design of experiments theory. In a later section of this chapter, the tuning of the activation functions in the pre-layers is performed with the full factorial design of experiments theory.

Table 21 List of the hyperparameters applied to the PINN method

Hyperparameters	**Value**
Training iteration	15000
Start learning rate	0.00001
Learning rate decay rate	10%
Hidden layer	[145,145,145,145, 1]
Pre-layer	[1,135]
Activation function	ELU
Optimizer for the adaptive normalization	Adam
Optimizer for model identification	L-BFGS-B
δ in (24)– (26)	0.9

After training the PINN method, the last 65% of the lithium-ion battery cell test is applied to test the PINN method. These are battery test data not exposed to the PINN method before the test process. For the test of the PINN method, maximum absolute error (MAE) and mean absolute error (Max AE) are performed. (35) and (36) provide the mathematical formula for MAE and Max AE.

$$MAE = \frac{\sum_{i=1}^{n}|y_i - x_i|}{n} \tag{35}$$

$$Max\ AE = Max(|y_i - x_i|) \tag{36}$$

In (34) and (35), n is the total number of data points, y_i is prediction, x_i is the true value, and $Max(\ )$is the maximum of the data.

3.4 ANN vs. PINN

A comparative study is conducted to review the effectiveness of the PINN method when data scarcity occurs. This comparative study compares five cases to evaluate the effect of the three PINN approaches: loss function modification, the adaptive coefficient in the loss function, and the PINN architecture. A list of the five cases is provided in Table 21. Two data insufficiencies are designed in the training and test data for the data scarcity. First, the training data size is limited to 35% of the battery cycle test. This proportion of the training data is less than in other ANN applications, in which the training data size is often greater than 50%. Second, because of the nature of the pulse cycle test data, there are many peaks in both train and test data. The train data contain one prominent and two small peaks in the battery temperature profile. The test data include three prominent and four small peaks in the battery temperature profile. At each peak, the slope changes quickly, creating the temperature profile's discontinuity or kink-like geometry. For accurate prediction at the peak or kink-like profile, the ANN methods often require dense training data size at that location [76], [81].

Table 22 Prediction accuracy of ANN, ANN variants, and PINNs

	MAE (ºC)	**MAX AE (ºC)**
ANN	4.00	59.53
ANN with loss function with unit coefficients	6.52	79.0
ANN with loss function with adaptive coefficients	6.83	95.0
PINN with the concatenated connection layer	0.06	0.50
PINN with the multiply connection layer	0.11	0.47

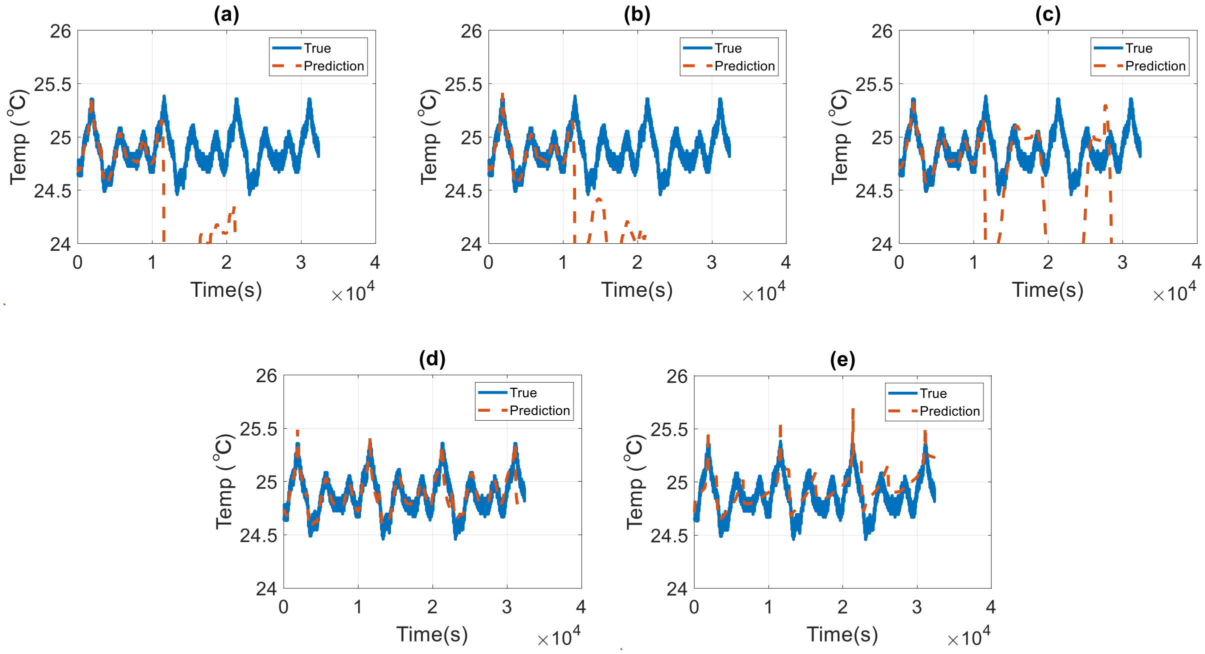

Fig. 21 Temperature predictions of various neural network approaches: (a) ANN, (b) ANN with loss function with unit coefficients, (c) ANN with loss function with adaptive coefficients, (d) PINN with concatenated layer, (e) PINN with multiply layer

In Fig. 21(a), temperature prediction by the ANN method is provided. The ANN cannot accurately predict the battery cell temperature in the test results. The ANN method correctly identifies no temperature peak in the test data. In Fig. 21(b), temperature prediction by the ANN method with loss function modification by adding physics law is presented. In the loss function, the coefficient is set to one in this case. In this case, the temperature prediction outcome slightly improved from the previous case. In the test, no peak in the battery temperature profile is accurately identified. Fig. 21(c) provides the temperature prediction by the ANN method with the loss function modification. In this case, the adaptive coefficients are implemented in the loss function. This method demonstrates some prediction improvement. The locations of all four small peaks are identified in the test temperature profile. However, the temperature predictions at the prominent peaks deviate largely from the true values, so the MAE of this case is the highest of all five cases. Fig. 21(d) presents the battery cell temperature predictions by the PINN method containing all three PINN approaches. In the PINN architecture, Fig. 21(d) has the concatenated layer as the connection layer. In the test results, the PINN method with the concatenated layer identified all peaks in the battery cell temperature profile with the lowest MAE. Lastly, in Fig. 21(e), the PINN architecture has the multiply layer as the connection layer. In this case, the PINN method identifies two large and small peaks with the lowest Max AE. However, the battery cell temperature predictions at the large peaks show a much larger prediction error than the PINN method with the concatenated layer. Table 21 contains the MAE and Max AE of all five cases considered in this study.

In conclusion, the PINN shows better prediction accuracy than the ANN and ANN variants, especially with data scarcity. This comparative study also demonstrates that without the presence of all three PINN approaches, the improvement in the prediction accuracy over ANN is not observable for the lithium-ion battery cell temperature prediction. It is also noted that incorporating the physics laws in the loss function, which is the most popular PINN approach, is not enough to improve the prediction outcome of the PINN method. This observation is also found in another study of the thermal application of the PINN method [76].

3.5 Effect of Pre-layer Activation Function and Connection Layer

In this section, the PINN method's pre-layer activation function and connection layer are optimized using the test plan designed by the full factorial design of experiments theory. For the pre-layer activation function, three different input variables are considered with two different activation functions: sine function and exponential function. These two activation functions are selected because they are in the specific analytical solutions for the differential equations. Also, it is assumed that the OCV and voltage will have the same pre-layer activation function based on the proximity of the two variables in the thermal equation. For the connection layer in the topology of the PINN architecture, the multiply and concatenate layers are considered in this study. Based on the full factorial design of experiments theory, a total of 16 test cases are generated. Table 23 shows the details of the 16 test cases.

Table 23 Test conditions for pre-layer activation function and connection layer optimization

Case #	**Pre-layer activation function**			**Connection Layer**
	Time	**Current**	**Voltage**	
1	sin	sin	sin	multiply
2	sin	sin	exp	multiply
3	sin	exp	sin	multiply
4	exp	sin	sin	multiply
5	exp	exp	sin	multiply
6	exp	sin	exp	multiply
7	sin	exp	exp	multiply
8	exp	exp	exp	multiply
9	sin	sin	sin	concatenate
10	sin	sin	exp	concatenate
11	sin	exp	sin	concatenate
12	exp	sin	sin	concatenate
13	exp	exp	sin	concatenate
14	exp	sin	exp	concatenate
15	sin	exp	exp	concatenate
16	exp	exp	exp	concatenate

Fig. 22 shows the temperature predictions made by the PINN architectures with the multiply layer. Significant prediction errors and considerable divergence between the temperature predictions and true values are observed from Case #1 to Case #5. For Case #6, reasonable prediction errors, MAE and Max AE, are produced. However, not all temperature peaks in the test data are correctly identified. In Case #7, significant prediction errors occurred, with the predictions diverging from the true values at the temperature peaks in the test data. Finally, in Case #8, the PINN method cannot find the two remote temperature peak locations in the test data.

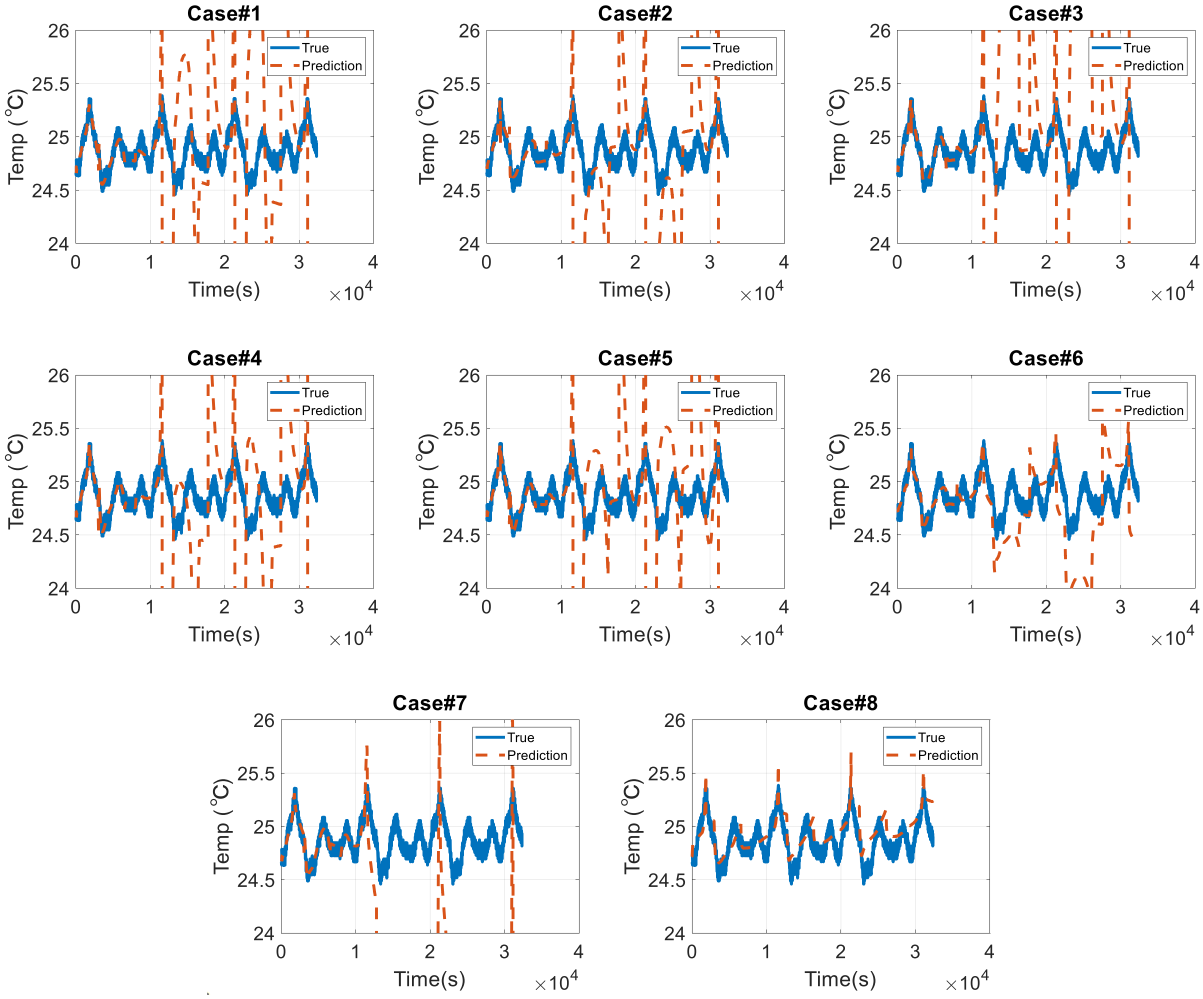

Fig. 22 Temperature predictions with the PINN methods with the multiply layer

Table 24 shows the MAE and MAX AE from Case #1 to Case #8, in which the multiply layer is implemented in the PINN architecture. Case #6 has the lowest MAE, and Case #8 has the lowest MAX AE.

Table 24 Prediction accuracy of PINN methods containing with the multiply layer

Case #	**MAE (ºC)**	**MAX AE (ºC)**
1	3.87	118.96
2	1.71	145.55
3	4.15	244.71
4	1.10	66.57
5	0.83	31.47
6	0.26	1.1
7	113.26	771.15
8	0.47	0.11

Fig. 23 shows the temperature predictions made by the PINN architectures with the concatenate layer. Case #9 has a significant prediction error without correctly identifying temperature peaks in the test data. Case #11 also could not predict the proper location of the three large temperature peaks, which created enormous prediction error. Case #10, #12, #13, and #15 find all temperature peak locations; however, the prediction error increases after a large peak where the rest time takes place. This rest location is another place where the current input data has a sudden slope change, requiring more data to learn the battery current and temperature behavior. Case #14 and Case #16 identify all temperature peaks in the test data and show no significant prediction error.

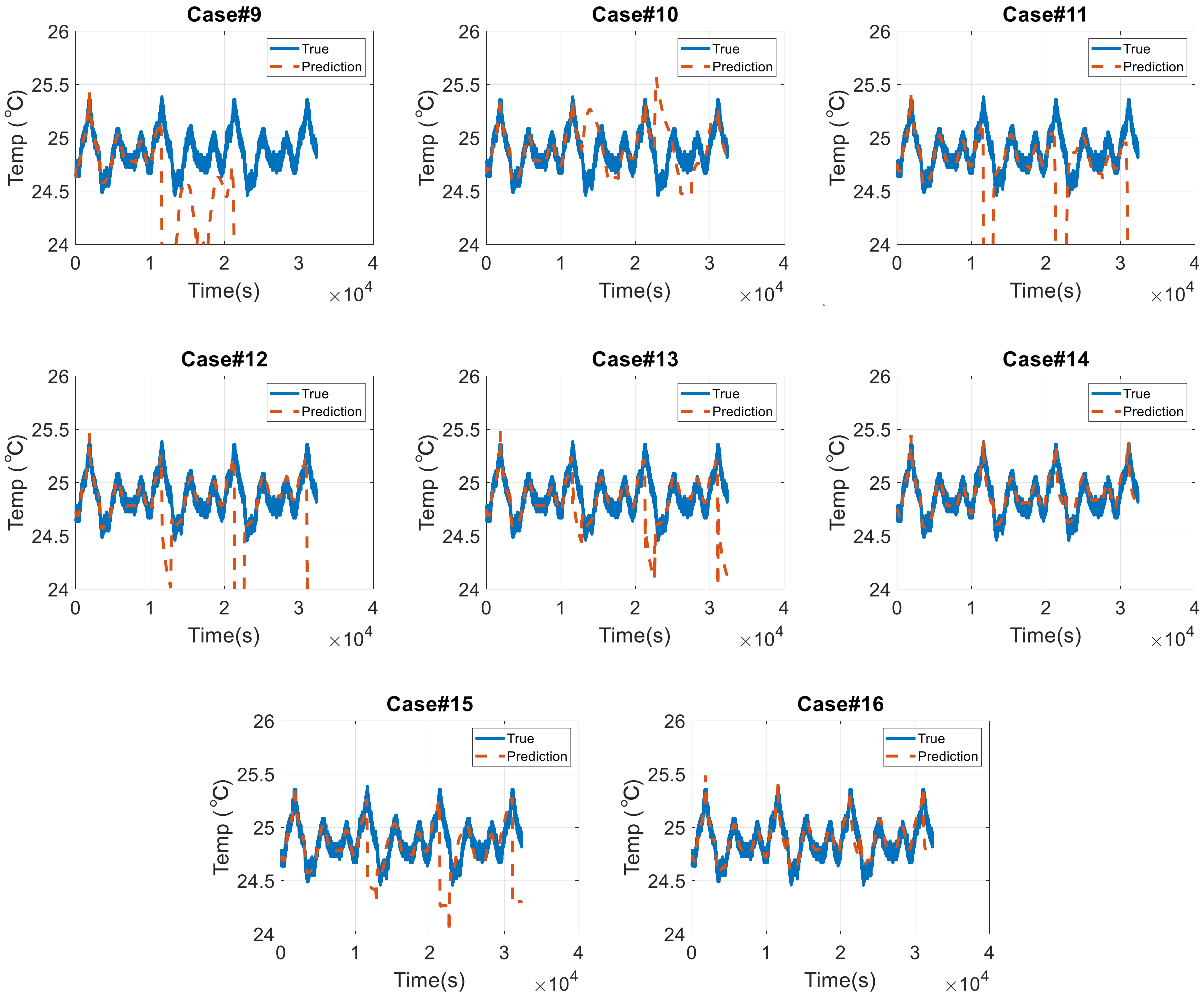
Case#9 Case#10 Case#11 Case#12 Case#13 Case#14 Case#15 Case#16

Fig. 23 Temperature predictions with the PINN methods with the concatenate layer

Table 25 shows the MAE and MAX AE from Case #9 to Case #16, in which the concatenate layer is implemented in the PINN architecture. Case #14 has the lowest MAE and MAX AE in all PINN architectures reviewed in this study. Therefore, the exponential activation function for the time, OCV, and voltage pre-layers and sine activation function for the current pre-layer with the concatenate layer connecting the pre-layer and hidden layer has the most accurate lithium-ion cell temperature prediction. Fig. 24 shows the PINN architecture that this study proposes.

Table 25 Prediction accuracy of PINN methods containing the concatenate layer

Case #	MAE (ºC)	MAX AE (ºC)
9	6.30	103.50
10	0.14	0.99
11	3.43	64.88
12	0.21	2.23
13	0.12	1.31
14	**0.05**	**0.31**
15	0.13	1.10
16	0.06	0.50

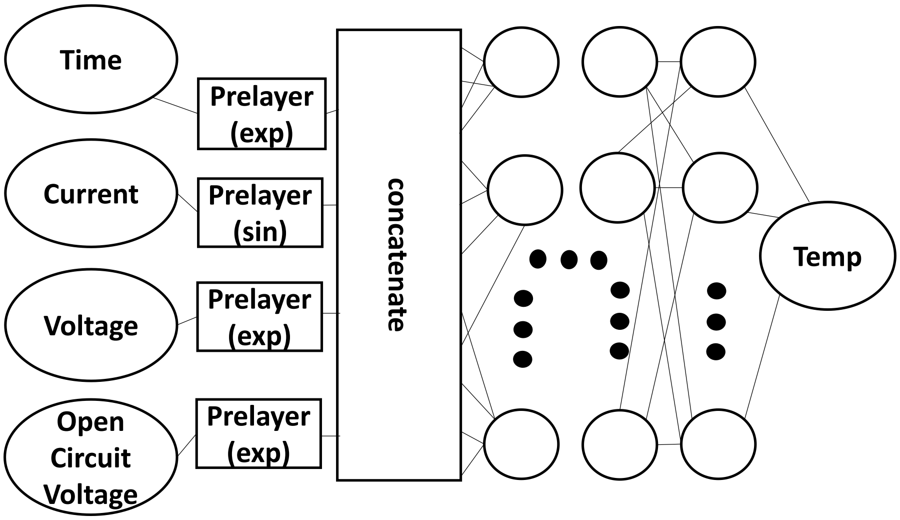

Fig. 24 Proposed PINN architecture

3.6 Conclusion

In this chapter, a PINN model is developed and proposed to predict the lithium-ion battery cell temperature during the constant charge and discharge cycle. The main novelties of this chapter are summarized as follows:

(1) A PINN model was developed by applying the battery thermal model to the loss function, implementing adaptive coefficients to the loss function, and modifying the

ANN architecture with the pre-layer and connection layer reflecting the analytical solution of the battery thermal model.

(2) A comparative study was conducted among PINN, ANN, and ANN variants to show that PINN is superior in predicting the battery cell temperature with limited data size and an unidentified battery thermal model.

(3) Further investigation was performed to optimize the PINN architecture and activation function in the pre-layer and connection layer to improve the accuracy of the prediction of the battery cell temperature. The investigation outcomes indicate that the PINN architecture with pre-layers containing the exponential activation functions for the time, battery voltage, and open-circuit voltage and containing the sine activation function for the current (Case #14) with a concatenated layer makes the highest prediction accuracy for the battery cell temperature. This study proposes this PINN architecture for predicting lithium-ion battery cell temperature.

In the next chapter, the PINN model developed in this chapter will be applied to the LSTM model introduced in Chapter 2 to predict the temperature distribution of the lithium-ion battery pack. This hybrid model is expected to ease the shortcomings of the LSTM model, which is based solely on the test data to train the LSTM.

Chapter 4 LSTM-PINN Hybrid Method for Lithium-ion Battery Pack Temperature Estimation

4.1 Introduction

Battery temperature distribution in a large-scale lithium-ion battery pack is critical for the safe and efficient use of the battery. According to the literature, nonuniform battery temperature distribution in the lithium-ion battery pack leads to power-capability, SOC, and capacity variation among the battery cells inside the battery pack [94]. This variation eventually causes localized battery degradation [95]–[96]. Also, the effect of the battery temperature distribution in the lithium-ion battery pack is intensified with the size of the battery current. Therefore, the battery temperature distribution must be controlled for the fast charging of the lithium-ion battery pack [97].

Despite the significance of the battery temperature distribution, the lithium-ion battery pack has space and cost constraints for placing temperature sensors inside the battery pack to obtain the temperature information for battery temperature control. Therefore, estimating the battery temperature distribution inside the battery pack is critical in order to overcome the limitations of the battery temperature measurement and improve the overall performance, safety, and life of the lithium-ion battery pack system.

Physics-based models and data-driven methods are two popular approaches in the literature to make temperature predictions in lithium-ion battery packs. For instance, in [98], the equivalent circuit battery model and battery thermal equations are incorporated to find the battery pack's temperature distribution. This method has several shortcomings. First, the model-based method is often not tolerant of inaccurate parameter identification and unaccounted model dynamics. Second, noise in the experimental data related to the model parameter identification is critical since a poorly fitted model could have a significant prediction error. Lastly, the convergence of the prediction by the model-based model without the initial condition is slow due to the large thermal mass of a large-scale lithium-ion battery pack.

On the other hand, the data-driven method is another approach to estimating the temperature distribution in the battery pack without the risks of the model-based approach. As discussed in Chapter 2, when the data-driven model has enough data to learn the thermal behavior of the lithium-ion battery pack, it can make accurate temperature predictions without the model identification, initial condition, and model fitting. In Chapter 2, the proposed data-driven method, LSTM, accurately predicts the battery temperature without system identification. However, training-data scarcity can cause less accurate prediction in the data-driven method. In Chapter 2, the LSTM model less accurately estimates the battery temperature in the middle of the battery module, with the training data containing the battery temperatures only at the ends.

In this chapter, improvement in the data-driven method to predict the battery pack temperature is proposed based on the LSTM application presented in Chapter 2. The proposed model combines the LSTM and PINN methods to enhance the robustness against data scarcity. As shown in chapter 3, the PINN method implements the physical law in the training process with the neural network architecture originating from the solution of the physics law. The physics model is expected to provide additional training to overcome the local data shortage. This chapter is organized as follows. Section 4.2 illustrates the thermal model applied to the PINN method. Section 4.3 elaborates the methodology with a general description of the proposed model and training process. Section 4.4 contains the results and discussion from various comparative studies to improve the PINN architecture and compares the temperature predictions made by the LSTM and the LSTM-PINN hybrid methods. Lastly, section 4.5 contains the conclusion.

4.2 Battery Thermal Model

As shown in Chapter 2, the LSTM model for battery pack temperature prediction has low battery-temperature accuracy at the location where the geometry of the battery module differs from the geometry of the battery pack temperature in the training data. A PINN method will be developed and later combined with the LSTM model to improve this limited temperature prediction capability. For this purpose, the geometric area where the PINN method is applied is limited to the battery module location. This location contains geometric data scarcity. The place where the PINN method is implemented is provided in Fig. 25. The exact figure describes the locations of the temperature measurements presented in the battery thermal model. Also, Fig. 26 shows a thermal resistance diagram of the PINN-applied area where the battery thermal model is formulated.

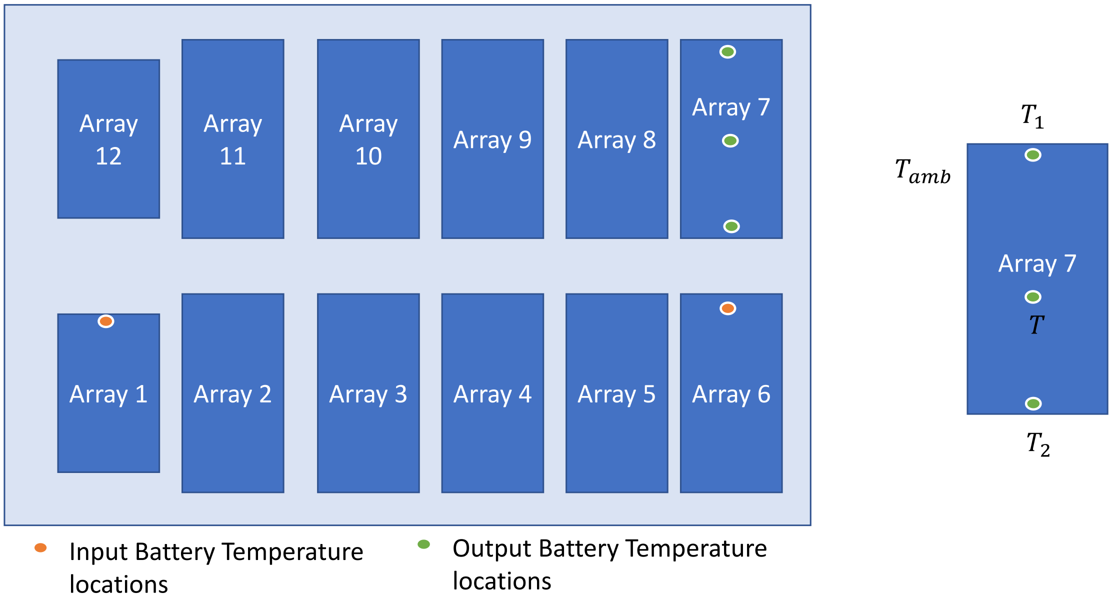

Fig. 25 Lithium-ion battery pack (left) and PINN-applied area (right)

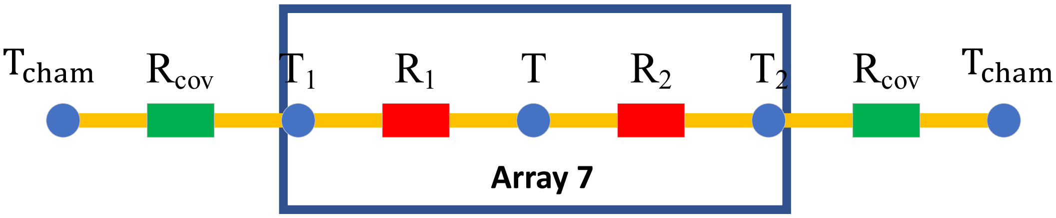

Fig. 26 Thermal resistance diagram at the PINN method-applied area (battery module #7)

In Fig. 26, T_{cham} is the chamber temperature around the battery module (array) #7. T_1 and T_2 are the battery temperatures at the ends of the battery module. T is the battery temperature in the middle of the battery module. R_1, R_2, and R_{cov} represent the thermal resistors between the two temperature locations. This thermal resistance diagram formulates the energy balance model in battery module #7. The model equation is provided in (37).

$$mC_p\frac{dT}{dt} = \dot{Q} + \frac{T-T_1}{R_1} + \frac{T-T_2}{R_2} + hA(T_1 + T_2 - 2T_{amb}) \tag{37}$$

In (37), m is the mass of battery module #7, C_p is the heat capacity of battery module #7, t is time, $\dot{Q}$ is the heat generation of battery module #7, h is the convective heat transfer coefficient, and A is the cross-sectional surface area. Reversible and irreversible heat generations are considered for battery heat generation in this study. One of the comparative studies in this chapter evaluates the effect of the physics law completeness, which is designed by adding reversible and irreversible heat generation terms to the battery thermal model. (38) and (39) show the mathematical equations for the reversible and irreversible heat generations [99].

$$\dot{Q}_r = IT\frac{dV_{ocv}}{dT} \tag{38}$$

$$\dot{Q}_{ir} = (V - V_{ocv})I \tag{39}$$

In (38) and (39), $\dot{Q}_r$ is reversible heat generation, $\dot{Q}_{ir}$ is irreversible heat generation, I is the battery current, T is the battery temperature, and V_{ocv} is the battery OCV. In this study, V_{ocv} is obtained from the SOC and OCV tables for various temperatures provided by the battery manufacturer. Therefore, heat generation contains reversible and irreversible heat generations (40).

$$\dot{Q} = IT\frac{dV_{ocv}}{dT} + (V - V_{ocv})I \tag{40}$$

With this battery thermal model, two thermal equations are formulated for the PINN method in the comparative study. (41) is the thermal equation with only irreversible heat generation, and (42) is the thermal equation with both reversible and irreversible heat generations.

$$f_{ir} = \frac{dT}{dt} - \lambda_1 (V - V_{ocv}) I - \lambda_2 (T - T_2) - \lambda_3 (T - T_1) + \lambda_4 (T_{amb} - T_2) + \lambda_5 (T_{amb} - T_1) = 0 \tag{41}$$

$$f_{re_{ir}} = \frac{dT}{dt} - \lambda_1 \left((V - V_{ocv}) I + IT \frac{dV_{ocv}}{dT} \right) - \lambda_2 (T - T_2) - \lambda_3 (T - T_1) + \lambda_4 (T_{amb} - T_2) + \lambda_5 (T_{amb} - T_1) = 0 \tag{42}$$

In (40) and (41), λ_1, λ_2, λ_3, λ_4, and λ_5 are the coefficients in the thermal equations that will be optimized during the training process using the backpropagation method.

4.3 Method

4.3.1 LSTM-PINN Hybrid Model

The LSTM-PINN hybrid model uses the LSTM model discussed in chapter 2 to predict the battery temperatures at the end sides of the battery module, T_1 and T_2, where the LSTM model shows high accuracy. However, for the temperature at the center of the battery module, T, the LSTM-PINN hybrid model implements the PINN method to predict the temperature. The overall schematic of the hybrid model is provided in Fig. 27. Also as shown in Fig. 27, the prediction outputs of the LSTM model feed into the PINN model after the normalization.

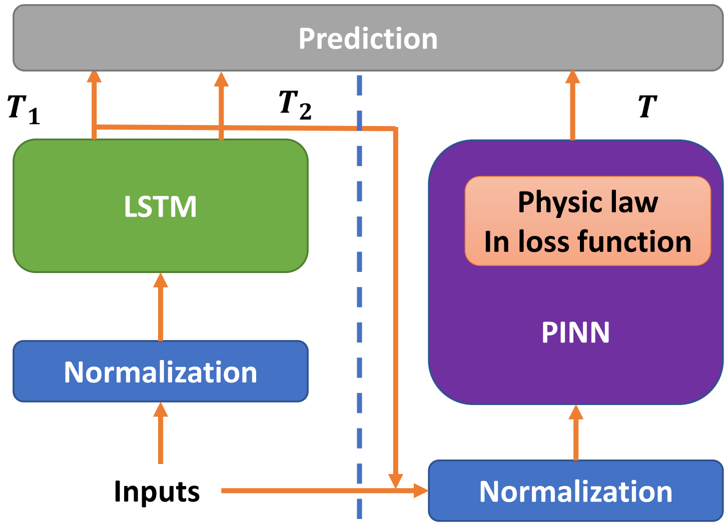

Fig. 27 Overview of LSTM-PINN hybrid model

4.3.2 Training

The details of the battery test and data acquisition can be found in section 2.4.2 of this paper. Before the training process, the obtained data are normalized between 0 and 1 as (15) in 2.4.3. During the training, the LSTM model is trained first with the hyperparameter provided in Table 16. Then the PINN model is trained with the battery test data and the outputs from the LSTM model. The hyperparameters implemented in the training process of the PINN model are listed in Table 26. After the training process, the LSTM-PINN hybrid predicts the lithium-ion battery pack temperatures in the test datasets, which are not applied to the training process. The root mean square error (RMSE) is calculated for the prediction error evaluation. The mathematical equation of RMSE is given in (43).

$$RMSE = \sqrt{\frac{\sum_{i=1}^{N}(x_i - \hat{x}_i)^2}{N}} \tag{43}$$

In (42), N is the total number of the data in the test datasets, i is the variable, $x_i$is the true temperature values, and $\hat{x}_i$ is the predicted temperature values.

Table 26 List of hyperparameters applied to the PINN portion of the LSTM-PINN model

Hyperparameters	Value
Training iteration	15000
Start learning rate	0.00001
Learning rate decay rate	10%
Pre-layer	[1,135]
Activation function	ELU
Optimizer for the adaptive normalization	Adam
δ in (24)– (26)	0.9

4.4 Results and Discussion

With the aforementioned LSTM-PINN hybrid model, this study conducts various comparative studies to enhance the temperature predictions in the middle of battery module #7 and to compare the prediction accuracy between the LSTM-PINN model and the LSTM model described in Chapter 2. The first comparative study and second full factorial design of the experiment study are presented to optimize the PINN architecture and hyperparameters for the LSTM-PINN hybrid model. Then the third comparative study evaluates the completeness effect in the battery thermal equation. Two battery thermal models prepared earlier in this chapter with two different battery heat generation methods, reversible and irreversible, are applied to the LSTM-PINN hybrid model to assess how completeness in the battery thermal equation would improve the LSTM-PINN model predictions. Lastly, the fourth comparative study compares the LSTM-PINN hybrid and the LSTM models introduced in Chapter 2.

4.4.1 Chamber Temperature Input to PINN

In the first comparative study presented in this chapter, the PINN architecture in the LSTM-PINN hybrid model is modified to cope with the different chamber temperatures in the lithium-ion battery pack test data. The input layer does not include the chamber temperature in the PINN architectures developed in Chapter 3 and [76] since all test data have the same chamber temperature. However, in the case of the PINN architecture for the battery pack temperature predictions in this chapter, the chamber temperature is an essential input due to the variation in the chamber temperature in the battery test data. Fig. 28 shows the proposed PINN architecture with the chamber temperature input.

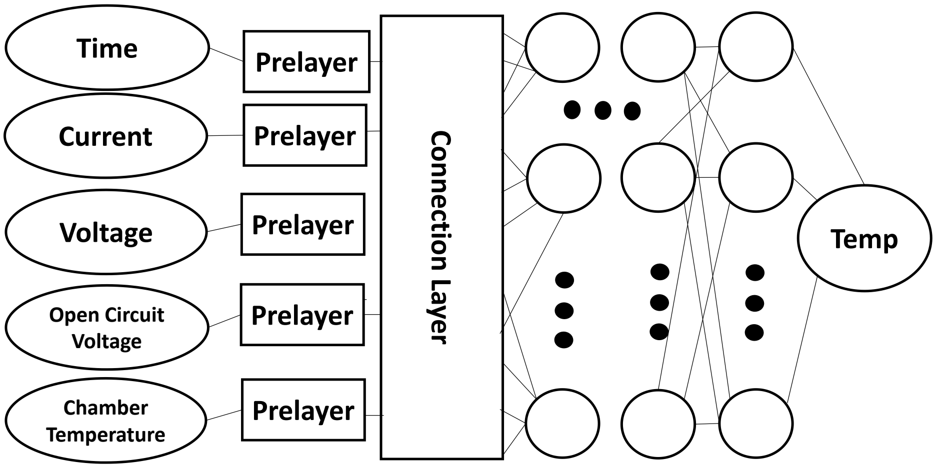

Fig. 28 PINN architecture with the chamber temperature input

Therefore, in the comparative study, three different cases are compared with each other. In the first case, the PINN architecture from Chapter 3 is directly applied to the LSTM-PINN hybrid model to make the battery temperature predictions at the center of battery module #7. In this PINN architecture, there is no chamber temperature in the input layer. In the second case, the PINN architecture presented in Fig. 28 is applied to the LSTM-PINN hybrid model with the sine activation function in the pre-layer connected to the chamber temperature input layer. In the third case, the PINN architecture presented in Fig. 28 is applied with the exponential activation function for the pre-layer.

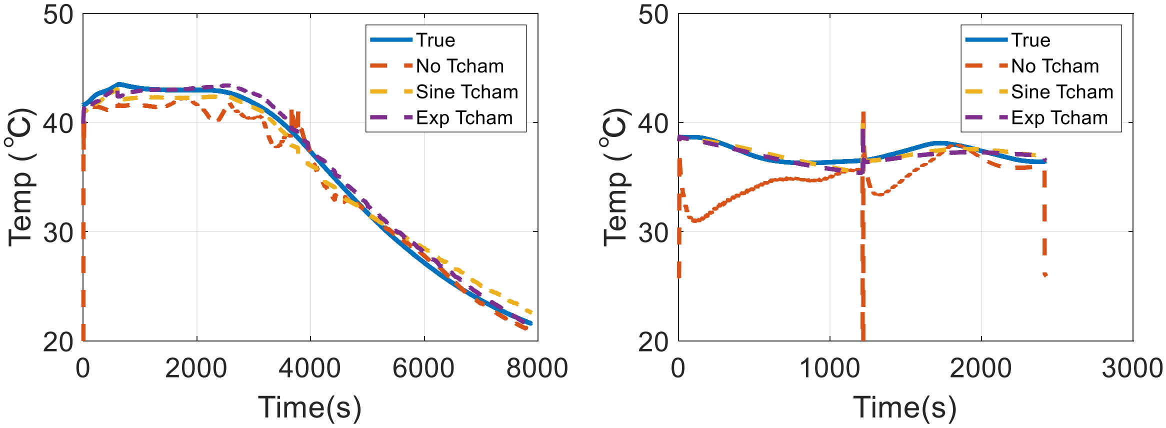

Fig. 29 LSTM-PINN hybrid model temperature predictions with the three different PINN architectures (No T_{cham}: first case, sine T_{cham}: second case, and exp T_{cham}: third case) for the DCFC profile (left) and the GL100 (right)

In Fig. 29, the temperature predictions from the three cases and the true temperature values are plotted for the DCFC and GL100 profiles designated for the LSTM-PINN hybrid model test. The figure shows that the temperature predictions made by the LSTM-PINN hybrid model with the PINN architecture excluding the chamber temperature input layer show more prediction errors than in the other two cases. This result supports the PINN architecture with the chamber temperature input layer for the LSTM-PINN hybrid model. Table 26 lists the prediction errors (RMSE) of all three cases. Table 27 indicates that between the two LSTM-PINN hybrid models including the chamber temperature in the input layer, the one with the exponential activation function demonstrates more accurate temperature prediction in the DCFC profile and similar prediction error in the GL 100 profile. In conclusion, this study proposes the LSTM-

PINN hybrid models including the chamber temperature in the input layer with the exponential activation function in the pre-layer for battery temperature prediction.

Table 27 List of hyperparameters applied to the PINN portion of the LSTM-PINN model

Case	**RMSE error (°C) for the battery temperature predictions at the center of the battery module #7**	
	GL 100 profile	**DCFC profile**
No T_{cham} pre-layer	3.43	1.03
T_{cham} pre-layer with sine activation function	0.47	0.96
T_{amb} pre-layer with exp activation function	0.52	0.57

4.4.2 Neuron Number and Hidden Layer Number Tuning

In the LSTM-PINN hybrid model, the neuron number and hidden layer number are two hyperparameters that must be tuned to make accurate battery temperature predictions. In this section, the tunning of two hyperparameters is conducted with the test conditions defined by the complete factorial design of experiments theory (DOE). Before this test run, pre-screen experiments were performed to find the range and level of each hyperparameter. For the neuron number, five levels in the test conditions range between 45 and 65. For the hidden layer number, the level is 4 and the range is between 3 and 6. Tables 28 and 29 contain the prediction error (RMSE) for the test conditions using the DCFC and GL100 test drive profiles. Both tables consider the temperature predictions only at the center of battery module #7.

Table 28 RMSE of the test conditions defined by the DOE for the DCFC drive profile

RMSE (°C)		Neuron # per layer				
		45	50	55	60	65
Hidden layer #	3	1.25	0.92	2.45	2.14	1.25
	4	1.25	2.50	0.84	1	1.86
	5	2.2	1.37	0.91	0.57	2.51
	6	1.63	1.27	1.26	3.05	1.78

Table 29 RMSE of the test conditions defined by the DOE for the GL100 drive profile

RMSE (°C)		Neuron # per layer				
		45	50	55	60	65
Hidden layer #	3	0.53	0.52	0.48	0.5	0.46
	4	0.45	0.55	0.45	0.49	0.6
	5	0.54	0.52	0.53	0.52	0.56
	6	0.54	0.66	0.52	0.79	0.5

In the test results of the DCFC drive profile, a neuron number of 55 per hidden layer and 4 hidden layers shows the lowest prediction error. The test results of the GL100 drive profile show no significant prediction error change. Thus, this study proposes the LSTM-PINN hybrid model with the neuron number of 55 per hidden layer and 4 hidden layers in the PINN architecture for the lithium-ion battery pack temperature predictions. Fig. 30 presents the proposed PINN architecture. For the following two sections in this chapter, the LSTM-PINN hybrid model with the proposed PINN architecture is applied to the comparative studies to show the influence of the completeness of the battery thermal model on the battery prediction accuracy and to compare the prediction accuracy between the LSTM-PINN hybrid model and LSTM model.

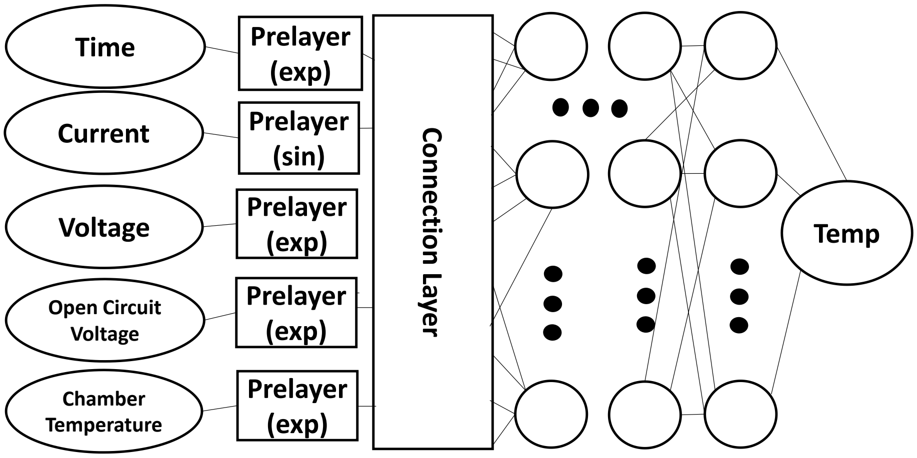

Fig. 30 Proposed PINN architecture for the LSTM-PINN hybrid model

4.4.3 Effect of Physics Model Completeness

The comparative study presented in this section evaluates the effects of the physics model completeness on the LSTM-PINN hybrid model. The physics model completeness is enhanced by adding reversible heat generation to the battery thermal model. Therefore, there are two cases for this comparative study. In the first case, the battery thermal model has no reversible heat generation term. (40) in 4.2 will be applied to the LSTM-PINN hybrid model. The battery thermal model has a reversible heat generation term in the second case. (41) in 4.2 contains the thermal model equation implemented in the LSTM-PINN hybrid model for the second case. Fig. 31 shows the true battery temperature values and temperature predictions at the center of battery module #7 by the methods described in both cases.

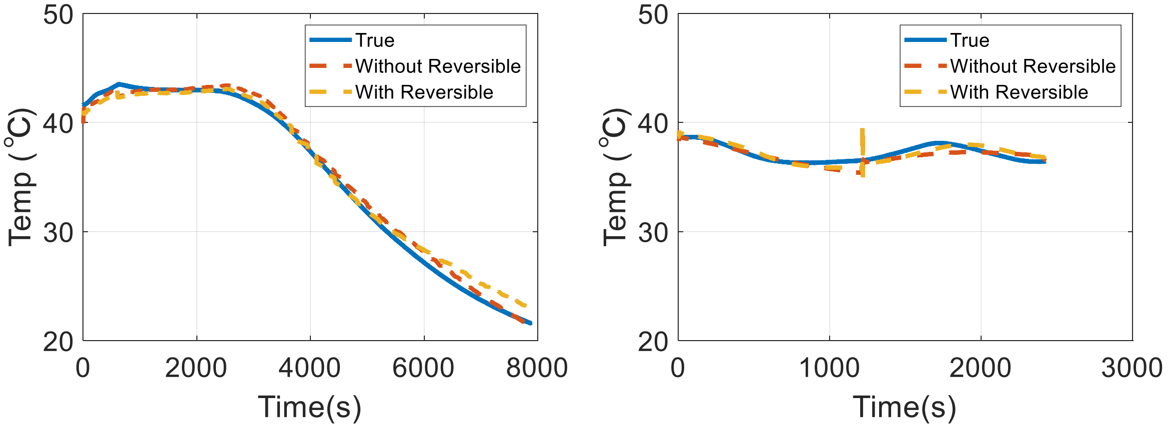

Fig. 31 Battery temperature predictions and true values for the DCFC profile (left) and the GL100 (right)

Table 30 RMSE from the comparative study for the physics model completeness

	RMSE (°C)	
Case	DCFC test profile	GL100 test profile
Hybrid model with only irreversible heat generation	0.57	0.52
Hybrid model with both reversible and irreversible heat generations	0.84	0.44

In Fig. 31, the battery temperature prediction error for the LSTM-PINN hybrid model containing only irreversible heat generation is less than that of the LSTM-PINN hybrid model containing both irreversible and reversible heat generations for the DCFC test profile. An opposite observation is made for the GL100 profile. However, the prediction error (RMSE) difference between the two cases for the DCFC test profile is 0.27°C, and the prediction error (RMSE) difference for the GL100 test profile is 0.08°C. The benefit of adding more completeness to the thermal model shown in the GL100 test profile is less than the increase of the prediction error in the DCFC test profile. Also, the GL 100 test profile has no divergence in the battery temperature prediction. However, in the DCFC test profile, the LSTM-PINN hybrid model containing both irreversible and reversible heat generations shows divergence at the end of the test profile. Therefore, in this study, the physics law with more completeness does not enhance the prediction accuracy. Moreover, this result shows the hybrid model's acceptance of the incomplete physical law.

4.4.4 LSTM-PINN Hybrid Method vs. LSTM

The comparative study presented in this section compares the battery temperature prediction errors of the LSTM-PINN hybrid model and the LSTM model. As discussed in Chapter 2, the LSTM model relies solely on the training data to learn the problem. Fig. 32 shows the battery temperature predictions by both models at the center of battery module #7 with the true temperature values for the DCFC and GL100 test profiles. The LSTM-PINN hybrid model predicts the battery temperature with a lower prediction error than the LSTM model does for the DCFC test profile, especially at the end of the profile. The performance of both models for the GL 100 test profile is similar. The prediction errors (RMSE) of both models for the two test profiles are tabulated in Table 31.

Table 31 RMSE from the LSTM model and LSTM-PINN hybrid model

	RMSE (°C)	
Case	DCFC test profile	GL100 test profile
Only LSTM	1.01	0.48
LSTM-PINN hybrid model	0.57	0.52

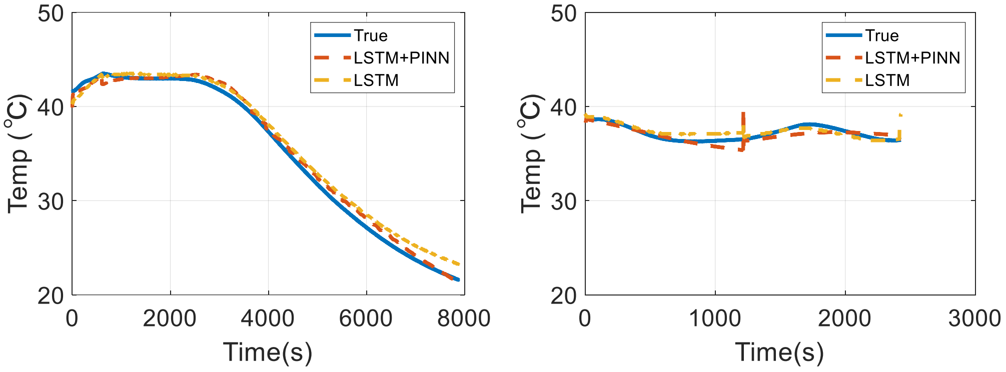

Fig. 32 Battery temperature predictions and true values for the DCFC profile (left) and the GL100 (right)

Observation demonstrates that the proposed LSTM-PINN hybrid model outperforms the LSTM model for battery pack temperature prediction. Also, this strength of the LSTM-PINN hybrid model is enhanced for the case with the long duration profile containing a considerable temperature variation, which is the DCFC profile in this study. The DCFC profile's battery pack temperature predictions for both models are listed in Table 32.

Table 32 RMSE of the battery pack temperature predictions by the LSTM model and LSTM-PINN hybrid model for the DCFC profile

(°C)	LSTM	LSTM-PINN hybrid
Output temp (end 1)	0.64	0.64
Output temp (middle)	1.01	0.57
Output temp (end 2)	0.40	0.4

4.5 Conclusion

In this chapter, an LSTM-PINN hybrid model is developed and proposed to predict lithium-ion battery pack temperatures. Unlike other prediction approaches such as a physics-based or a data-driven model, this LSTM-PINN hybrid model takes advantage of both physics-based and data-driven models by implementing the PINN method to incorporate the physics laws during the training of the data-driven method. The main novelties of this chapter are summarized as follows:

- The proposed LSTM-PINN hybrid model has a unique PINN architecture, with input layers designed for the chamber (ambient) temperature variation in the battery data.

- The proposed LSTM-PINN hybrid model shows robustness against the incompleteness of the battery thermal model, which includes missing terms and a less descriptive physics model.

- When data scarcity occurs, the proposed LSTM-PINN hybrid model gives more accurate predictions than the LSTM model. For instance, the geometric location of the temperature predictions is different from the temperature information in the training data. In the case presented in this chapter, the strength of the proposed LSTM-PINN hybrid model is significant when the predicted temperature variation increases and the profile duration is extended.

Chapter 5 Data Driven Battery Model Parameter Identification

5.1 Introduction

As proposed in the literature, the model-based approach is an effective method for estimating the behavior of the lithium-ion battery. Moreover, it is often implemented in the lithium-ion battery control methodology. The model-based approach contains lithium-ion battery models consisting of mathematical equations describing the internal processes in the battery. For instance, in the equivalent circuit model (ECM), electrical circuit equations analogous to the lithium-ion battery internal mechanism and producing similar responses such as the battery voltage are formulated to simulate the battery behaviors. The pseudo-two-dimensional lithium-ion battery model contains mathematical governing equations describing mass conservation, charge conservation, and electrochemical reactions at both electrodes and electrolytes. Lithium-ion battery models, both physics-based and empirical, implement mathematical equations at various complexity levels, including ordinary and partial differential equations, to predict the battery behaviors and characteristics. Therefore, accurately identifying the battery model equations is critical to enhancing the prediction quality.

A data-driven method such as ANN can be implemented to identify the lithium-ion battery model equations. Compared to other system-identification methods, the black-box approach avoids fitting the complex mathematical equations and performing destructive battery tests. However, the data-driven method has a shortcoming related to the data size to maintain highly accurate system identification. This chapter will examine various sampling methods such as Plackett-Burman and Latin hypercube for their effectiveness in reducing the data size while maintaining the prediction accuracy without a dramatic increase in prediction error.

This chapter is organized as follows. Section 5.2 includes a literature review on the methods to identify the lithium-ion battery models. Section 5.3 contains the methods section. Section 5.4 reviews the results of the comparative study to evaluate various sampling methods for the ANN to identify the battery models. Lastly, section 5.5 includes the conclusion.

5.2 Literature Review

Although battery model parameter identification is critical to enhancing the performance of the lithium-ion battery model, it is difficult to identify the battery model parameters. The battery manufacturers are reluctant to release related information, and most battery parameters are hard to measure, especially with non-destructive methods. Also, the lithium-ion battery's highly nonlinear behavior increases the difficulty of identifying the battery model parameters with the fitting methods [100]. Researchers have attempted to develop methods to identify the lithium-ion battery model parameters, as documented in the literature. In [101], the author implemented a least-squares framework-based fitting method to identify the parameters of the single particle battery model. In [102], the author developed a genetic algorithm-based method to identify 88 battery model parameters of the pseudo-two-dimensional lithium-ion battery model. The study presented in [103] proposed a model-fitting method to identify the kinetics-related parameters of the pseudo-two-dimensional lithium-ion battery model.

Furthermore, a group of researchers conducted studies to implement deep learning-based methods to identify the battery parameters. In [104], an ANN approach was developed to predict Li-ion diffusion coefficients at anode and cathode, reaction rate coefficients at anode and cathode, and solution phase resistance. These material battery parameters partially identify the single-particle battery model. This study generated 3125 datasets based on full factorial experiment design theory (i.e., five factors and five levels) to train the ANN. All datasets were synthesized by the single particle battery model with the 1C discharge current profile. In the study presented in [105], an ANN structure was developed to predict cathode initial concentration at the beginning of discharge, cathode conductivity, volume-specific capacity of the anode, volume-specific capacity of the cathode, and diffusion coefficients of electrolyte, anode, and cathode. These variables are a subset of the coefficients in the mathematical equations in the pseudo-2-dimensional Li-ion battery model. This study generated 2657205 datasets based on full factorial experiment design theory (i.e., 12 factors and three levels with five different discharge rates) from the simulation with the pseudo-2-dimensional Li-ion battery model. Unlike the previous paper, this paper generated datasets with various discharge rates. Lastly, Chun et al. published several papers regarding battery model parameter estimation. In [106], a convolution neural network (CNN) combined with ANN was developed to estimate the battery degradation related to the battery model parameters: two solid-particle surface areas (cathode, anode), two solid-particle conductivities (cathode, anode), SEI layer resistance, and electrolyte diffusivity. This study generated 73728 datasets with the pseudo-2-dimensional Li-ion battery model for training, validating, and testing the ANN. In [107], the authors developed an LSTM combined with ANN to estimate the battery degradation related to the battery model parameters: two solid-particle surface areas (cathode, anode), two solid-particle conductivities (cathode, anode), SEI layer thickness, and normalized available capacity. This study generated 179180 datasets with the pseudo-2-dimensional Li-ion battery model for training, validating, and testing the neural network architecture. In this study, the authors used a 100-second current profile in the data generation.

In summary, the data-driven methods for battery model parameter identification in the literature followed the process described in Fig 33. It begins with defining the battery model parameters needing to be identified with the range of the battery parameters. Then, the battery model parameters combinations are designed based on the sampling methods, such as the full factorial design of experiments methods. After this, the determined combinations of battery model parameters and inputs such as current and temperature are applied to the lithium-ion battery model to produce training and validation data for the neural network. After the training and validation of the neural networks, the test process is conducted with a new data set.

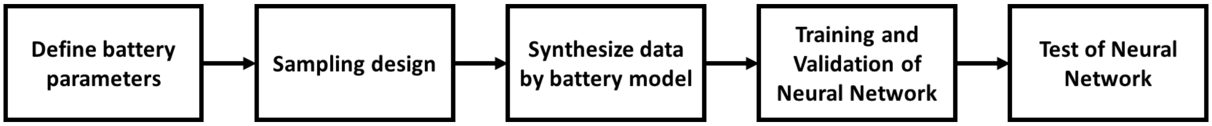

Fig. 33 Work process for the data-driven battery model parameter identification

It is notable from the literature that although all studies utilizing the data-driven methods successfully identified the battery model parameters, they were able to identify only a partial portion from the entire set of battery model parameters. Primarily, less than ten battery model parameters were investigated. This limitation was mainly due to the implementation of the full factorial design of experiments theory for the training data design. This design method often requires a large data size, which limits the total quantity of identifiable battery models. In the case of identifying a large group of lithium-ion battery model parameters, such as more than ten battery parameters, it is not practically feasible to apply the full factorial sample design method due to the time and computation power constraints. For this case, this chapter examines implementing other sampling design methods such as Plackett-Burman and Latin hypercube methods to keep the training data size manageable to create while incurring only a slight prediction error increase.

5.2.1 Sample Design Methods

Sampling design methods are a critical step in data-driven battery model parameter identification since they map the information that will train the neural networks. As discussed in the previous section, the literature's most popular sample design method is the full factorial design of experiments theory. In this theory, all sample combinations cover all vertices of the cube plot in which the side of the cube represents the range of each battery model parameter [108]. For n model parameters and k levels, this design of experiments theory maps sample combinations in a manner such that the total number of the sample combinations is provided as (44).

$$\text{\# of test combination} = \mathrm{n}^{\mathrm{k}} \tag{44}$$

With this characteristic of the full factorial design of experiments theory, it is not an acceptable sample design method for identifying the entire set of the battery model parameters because it designs an enormous number of sample combinations that are not practically possible to synthesize from the battery model. Table 33 shows the total number of sample combinations designed by the full factorial design of experiments theory.

Table 33 Total number of the sample combinations designed by the full factorial design of experiments theory

Parameter number	3-level	5-level
2	9	25
3	27	125
4	81	625
5	243	3125
6	729	15625
7	2187	78125
8	6561	390625
9	19683	1953125
10	59049	9765625

According to Table 33, if a study identifies ten battery model parameters, the 5-level full factorial design of experiments theory maps 9765625 sample combinations needing to be generated by a battery model. Assuming that the battery model takes one minute to generate one sample, the total time required to generate all required samples is 6782 days. The same calculation for the 3-level full factorial design of experiments theory is 41 days.

Plackett-Burman (PB) and Latin hypercube (LH) sampling methods are two alternate sampling methods that could replace the full factorial design of experiments theory. The PB sample method is one of the fractional factorial design of experiments methods. This method executes only a 2-level (min and max) sample design. Also, it maps the total sample size equal to a multiple of four. LH sampling is another type of sample design method in which the user defines the total sample size. In this method, square grids are constructed based on the sample size so that the row and column numbers are equal to the sample size. Then sample combinations are randomly located, so each row and column in the square grids contains only one sample combination. In each sample combination location, the exact sample combination is determined by the inverse of the cumulative distribution function. In equation (45), $x_{i,k}$ is the kth sample of the factor, i. F is the cumulative distribution function. Moreover, N is the sample size [109].

$$x_{i,k} = F_i^{-1}\left(\frac{k-0.5}{N}\right) \tag{45}$$

Fig. 34 presents the 3-level full factorial, PB, and LH (sample size of 3) design of experiments methods for two battery model parameters. As the figure indicates, the full factorial method contains the sample combination at both boundaries and inside the boundary of the range of the battery model parameter. In PB, the sample combinations are available only at the boundary, and in LH, the sample combinations are located only inside the boundary. This chapter proposes combining PB-LH sample methods with the PB and LH sample methods. In the combined PB-LH sample design method, the sample combinations are placed both in the boundary and inside of the boundary defined by the range of the battery model parameter.

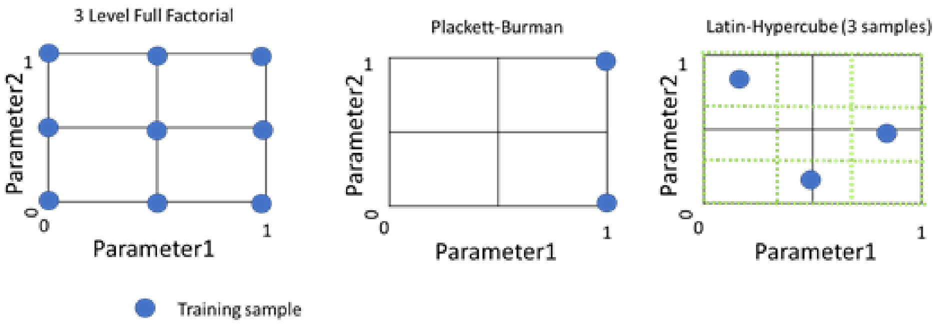

Fig. 34 Full factorial (left), Plackett-Burman (middle), and Latin hypercube sampling (right) for 2 factors (parameters)

5.2.2 Pseudo Two-Dimensional (P2D) Lithium-Ion Battery Model

The P2D lithium-ion battery model is a volume average and microscale physics model using a gradient in the two dimensions of between the two electrodes and the radial direction of the electrode particles. This model consists of governing equations describing the physical phenomena at the electrodes and electrolytes. In this study, the battery simulation data are created by the P2D lithium-ion battery model to train the LSTM method. Table 33 contains the governing equations with the boundary conditions of the P2D lithium-ion battery model. Fig. 35 shows the schematic of the P2D battery model. In addition to the governing equations, additional equations define the battery model’s internal variables such as open circuit potential. The additional equations used in the P2D battery model are listed in Table 34.

Table 34 Governing equations used in the P2D lithium-ion battery model

Name	Mathematical Equation	Boundary Condition
Mass conservation at the electrodes	$\frac{\partial c_s}{\partial t} = \frac{1}{r^2}\frac{\partial}{\partial r}\left(D_s r^2 \frac{\partial c_s}{\partial r}\right)$	$-D_s \frac{\partial c_s}{\partial r}\Big\vert_{r=0} = 0$ $-D_s \frac{\partial c_s}{\partial r}\Big\vert_{r=R_s} = j_n$
Electrochemical kinetics (Butler-Volmer equation)	$j_n = j_o \left[exp\left(\frac{\alpha_a F}{RT}\eta\right) - exp\left(\frac{-\alpha_c F}{RT}\eta\right)\right]$	-
Mass conservation in the electrolyte	$\frac{\partial(\varepsilon c)}{\partial t} = \frac{\partial}{\partial x}\left(D_{eff}\frac{\partial c}{\partial x}\right) + (1 - t_+) a j_n$ where $a = \frac{3}{R_s}(1 - \varepsilon - \varepsilon_f)$	$-D_{eff}\frac{\partial c}{\partial x}\Big\vert_{x=0\ and\ x=L_p+L_s+L_n} = 0$
Charge conservation at the electrodes	$\frac{\partial}{\partial x}\left(\sigma^{eff}\frac{\partial \phi_s}{\partial x}\right) = aFj_n$	$-\sigma^{eff}\frac{\partial \phi_s}{\partial x}\Big\vert_{x=0\ and\ x=L_p+L_s+L_n} = \frac{I}{A}$ $-\sigma^{eff}\frac{\partial \phi_s}{\partial x}\Big\vert_{x=L_n,\ L_n+L_s} = 0$
Charge conservation in the electrolyte	$\frac{\partial}{\partial x}\left(k^{eff}\frac{\partial \phi_e}{\partial x}\right) + \frac{2RT(1-t_+)}{F}\frac{\partial}{\partial x}\left(k^{eff}\frac{\partial c}{\partial x}\right) = aFj_n$	$-k^{eff}\frac{\partial \phi_e}{\partial x}\Big\vert_{x=0,\ L_n+L_s+L_p} = 0$

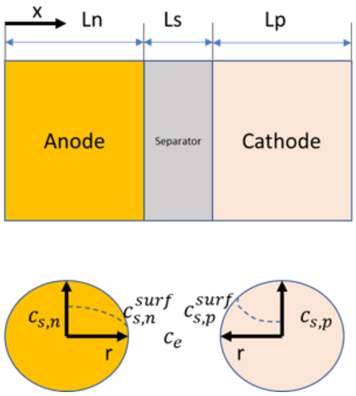

Fig. 35 Schematic overview of P2D lithium-ion battery model

Table 35 Additional equations

Name	Mathematical Equation
Exchange current densities at the electrode [110]	$j_o = k_0\left(c_s^{max} - c_s^{surf}\right)^{0.5} {c_s^{surf}}^{0.5} {c_s}^{0.5}$
Overpotential at the electrode	$\eta = \phi_s - \phi_e - U$
Open circuit potential at cathode	$V_{ocp} = -c_1 sto^4 + c_2 sto^3 - c_3 sto^2 + c_4 sto + c_5$
Electrolyte conductivity [111]	$\Sigma_e = 0.1297 \frac{c}{1000}^{3} - 2.51 \frac{c}{1000}^{1.5} + 3.329 \frac{c}{1000}$ $arrhenius = e^{\frac{E_{k_e}}{R\left(\frac{1}{298.15} - \frac{1}{T}\right)}}$ $Electrolyte\ conductivity = \Sigma_e \times arrhenius$
Cathode active material volume fraction	$v_{cathode,active} = 1 - \varphi_{cathode} - v_{im}$
Anode active material volume fraction	$num = t_{positive} \times c_{cathode,max} \times \left(1 - sto_{cathode,min}\right)$ $den = t_{negative} \times c_{anode,max} \times \left(1 - sto_{anode,min}\right)$ $v_{anode,active} = v_{cathode,active} \times np_{ratio} \times \frac{num}{den}$
Initial concentration in cathode	$c_{cathode,ini} = sto_{cathode,min} \times c_{cathode,max}$
Initial concentration in anode	$c_{anode,ini} = sto_{anode,max} \times c_{anode,max}$
Lithium-ion diffusivity in cathode [110]	$arrhenius = e^{\frac{E_{D_s,cathode}}{R\left(\frac{1}{298.15} - \frac{1}{T}\right)}}$ $D_{Li,cathode} = D_{ref,cathode} \times arrhenius$
Lithium-ion diffusivity in anode [112]	$arrhenius = e^{\frac{E_{D_s,anode}}{R\left(\frac{1}{298.15} - \frac{1}{T}\right)}}$ $D_{Li,anode} = D_{ref,anode}\left(1.5 - sto_{anode}\right)^{1.5} \times arrhenius$
Cathode exchange current density [12]	$arrhenius = e^{\frac{E_r,cathode}{R\left(\frac{1}{298.15} - \frac{1}{T}\right)}}$ $i_{o,cathode} = 2 \times m_{cathode,ref} \times arrenhenius \times \frac{c_e}{c_{e,max}}^{0.5} \times \left(\left(1 - \frac{c_{surf,cathode}}{c_{cathode,max}}\right)^{0.5} \frac{c_{surf,cathode}}{c_{cathode,max}}^{0.5}\right)$
Anode exchange current density [12]	$arrhenius = e^{\frac{E_{r,anode}}{R\left(\frac{1}{298.15} - \frac{1}{T}\right)}}$ $i_{o,anode} = 2 \times m_{anode,ref} \times arrenhenius \times \frac{c_e}{c_{e,max}}^{0.5} \times \left(\left(1 - \frac{c_{surf,anode}}{c_{anode,max}}\right)^{0.5} \frac{c_{surf,anode}}{c_{anode,max}}^{0.5}\right)$

5.3 Method

5.3.1 Impact of Data Sampling Methods

In order to evaluate the impact of data sampling methods on the data-driven battery model parameter identification, a study with four different data sampling methods is conducted with the LSTM method. Three-level full-factorial, PB, LH, and combined PB/LH design of experiments methods are implemented as the data sampling methods with sample sizes of 6561, 8, 10, and 18. Based on this sample design, training data are synthesized by the P2D lithium-ion battery model with a 5A constant discharge current to identify the eight battery model parameters: anode and cathode initial stoichiometries at the beginning of discharge, anode and cathode reference exchange current densities, anode and cathode solid diffusion coefficients, and anode and cathode active material volume fractions of a 5Ah Li-ion battery.

5.3.2 Battery Model Parameters

For the training data generation by the P2D battery model, 5Ah battery specifications are applied to the P2D battery model in addition to the unknown battery model parameters. Table 36 provides the 5 Ah battery specifications.

Table 36 5Ah battery specifications applied to all synthesized data

Battery model parameter	Value	Battery model parameter	Value
Electrode height (m)	0.089	Anode particle radius (m)	5E-6
Electrode width (m)	2.34	Cathode particle radius (m)	5.22E-6
Anode porosity	0.39	Initial concentration in electrolyte ($m \cdot m^{-3}$)	1200
Cathode porosity	0.416	Anode conductivity ($S \cdot m^{-1}$)	100
Separator porosity	0.46	Cathode conductivity ($S \cdot m^{-1}$)	100
Anode thickness (m)	4.46E-5	Cathode thickness (m)	4.55E-5
Anode chemistry	Graphite	Cathode Chemistry	NMC

Table 37 and Table 38 show the range of the unknown battery model parameters used in the sample design. In the case of the 3-level full factorial sample design, Table 37 contains the battery model parameter values at each level. For PB and LH, the maximum and minimum values of the unknown battery model parameters are provided in Table 38.

Table 37 The range of the unknown parameters applied to 3-level full factorial method

Level	Anode initial stoichiometries at the beginning of discharge	Cathode initial stoichiometries at the beginning of discharge
1	7.2E-1	3.6E-1
2	8E-1	4E-1
3	8.8E-1	4.4E-1
Level	Anode reference exchange current densities	Cathode reference exchange current densities
1	1.08E+1	1.8
2	1.2E+1	2
3	1.32E+1	2.2
Level	Anode solid diffusion coefficients	Cathode solid diffusion coefficients
1	1.35E-14	2.7E-14
2	1.5E-14	3E-14
3	1.65E-14	3.3E-14
Level	Anode active material volume fraction	Cathode active material volume fraction
1	0.54	0.405
2	0.6	0.45
3	0.66	0.495

Table 38 The range of the unknown parameters applied to Plackett-Burman and Latin hypercube methods

Level	Anode initial stoichiometries at the beginning of discharge	Cathode initial stoichiometries at the beginning of discharge
Min	7.2E-1	3.6E-1
Max	8.8E-1	4.4E-1
Level	Anode reference exchange current densities	Cathode reference exchange current densities
Min	1.08E+1	1.8
Max	1.32E+1	2.2
Level	Anode solid diffusion coefficients	Cathode solid diffusion coefficients
Min	1.35E-14	2.7E-14
Max	1.65E-14	3.3E-14
Level	Anode active material volume fraction	Cathode active material volume fraction
Min	5.4E-1	4.05E-1
Max	6.6E-1	4.95E-1

5.3.3 Experiment Plan

To test the performance of the LSTM networks, five new test datasets were generated by the P2D battery model. These datasets were not included in the training and validation datasets generated earlier. Figure 36 shows the overall test process conducted in this section of the paper. In the test process, the pre-selected battery model parameters of the five new test datasets were compared to the identified battery model parameters by the LSTM networks.

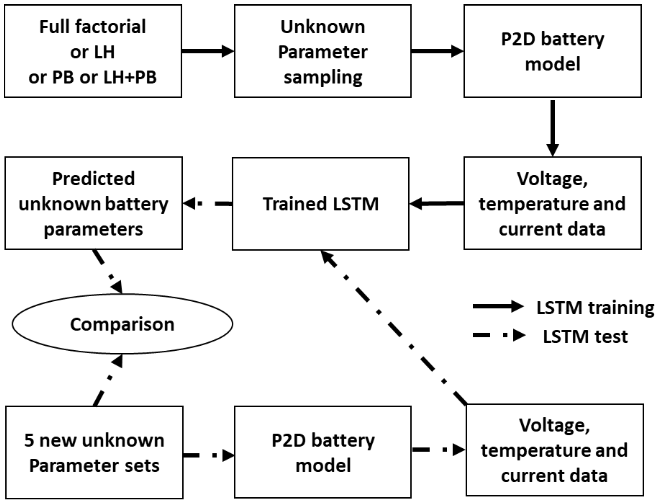

Fig. 36 LSTM test process

For the training and validation of the LSTM networks, 80 and 20%, respectively, of the data designed by the four sample design methods were applied. All data used in the training and validation were normalized, padded, and transformed to apply the five hundred seconds sliding window in the input data with a sampling rate of 100 seconds. For the hyperparameters of the LSTM network, 3 units in a single LSTM layer were used with a batch size of 5, a learning rate of 0.001 with Adam optimization, and an epoch size of 100.

5.3 Results and Discussion

The relative errors between the two values are computed to compare the true and identified parameters. In (46), the relative error applied in this study is formulated.

$$Relative\ error\ (\%) = \frac{|Prediction - True|}{True} \times 100 \quad (46)$$

Fig. 37 and Fig. 38 contain the relative errors for all eight battery model parameters with the four sample design methods. In the results, the LSTM networks trained with the data design by the 3-level full factorial design of experiments method have the lowest relative error compared with other LSTM networks trained with the data designed with the other three sample design methods. The worst-performing LSTM network is trained with the data designed by the LH method. On average, of all eight battery model parameters, the LSTM networks trained with the data designed by the 3-level full factorial sample design method have 1.91% less relative error than that of the LH method. The relative errors of the PB and PB/LH combined methods are located between the relative errors of the 3-level full factorial sample design method and the LH method. The anode diffusion coefficient is the parameter with the most considerable relative error difference between the 3-level full factorial sample design method and the LH method at 3.07%. The cathode initial stoichiometries at the beginning of discharge is the parameter identified with the most minor relative error difference.

Although prediction error increases with the LSTM network trained with data designed by the LH, PB, and LH-PB combined methods, the three sampling methods reduce the data sampling size by over 90%. To identify all battery model parameters of the P2D battery model, the three sample design methods could be applied to reduce the data sample size. However, it is also indicated from this study that the sample size reduction should be controlled to improve the accuracy of the parameter identification by the LSTM. In the case of the LH and LH-PB methods, the total sample number could be adjusted by increasing the sample number designed by the LH method.

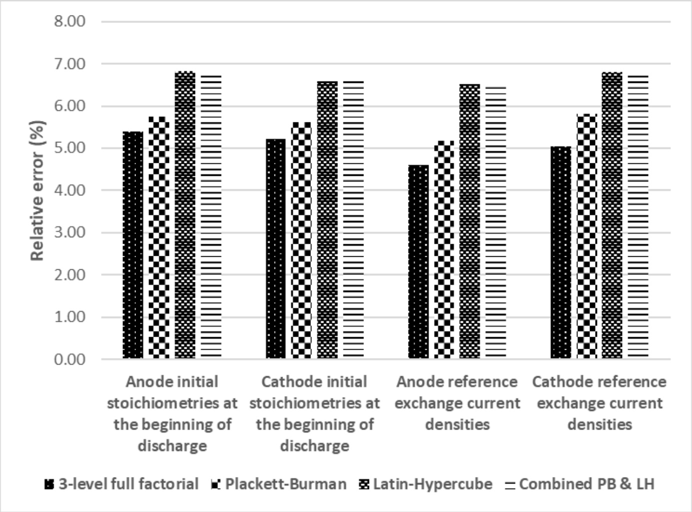

Fig. 37 Relative prediction errors from the LSTM trained with data design with different design of experiment methods (3level: 3-level full factorial, PB: Plackett-Burman, LH: Latin hypercube, PBLH: combined Plackett-Burman and Latin hypercube)

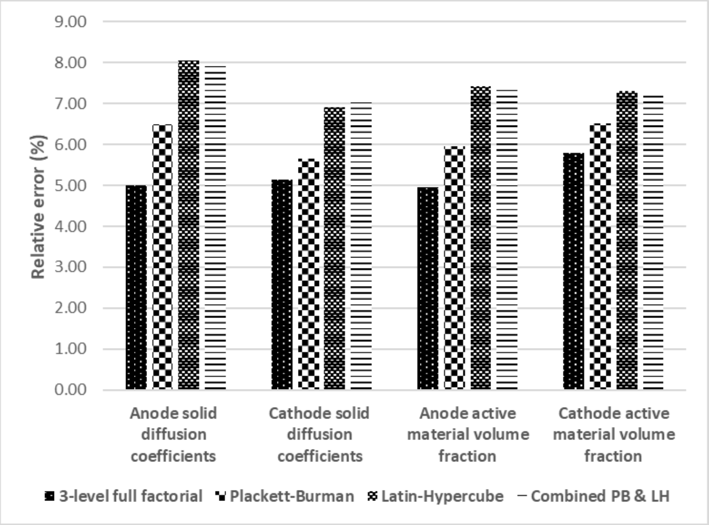

Fig. 38 Relative prediction errors from the LSTM trained with data generated from different design of experiment methods (3level: 3-level full factorial, PB: Plackett-Burman, LH: Latin hypercube, PBLH: combined Plackett-Burman and Latin hypercube)

5.4 Conclusion

This chapter conducted a comparative study to evaluate the effect of various data sampling methods for the LSTM method to identify the P2D battery model equations. This work estimates eight battery parameters from the P2D battery models. The eight parameters are selected for their relationship to the battery cell design, resistance, and diffusion. The main novelty of this chapter is summarized as follows:

- The results of the comparative study indicate that the LSTM trained with a significantly reduced number of sample data by the proposed PB, LH, and combined PB/LH can achieve good prediction accuracy (estimation error is increased by only 3% with over 90% reduction in data size compared to the 3-level full-factorial design approach).

The proposed sampling method is expected to identify more battery parameters from a complex battery model, such as the P2D battery model for model identification.

Chapter 6 Conclusions

6.1 Summary of Conclusions

The contributions in this dissertation are summarized as follows.

In Chapter 2, LSTM methods are proposed to predict the lithium-ion battery voltage and battery pack temperature. With the literature review and the comparative study to predict the lithium-ion battery voltage presented in this chapter, the LSTM method was elected as the most suitable ANN method due to its high prediction accuracy, fast convergence, and robustness against external temperature such as -30°C. With the proposed LSTM methods, lithium-ion battery voltage prediction at low temperature could be accurately performed, and the temperature distribution of the temperatures of the entire battery pack could be estimated with only a selected number of temperature measurements. All these predictions were made without the battery and thermal characterization information, which is sometimes not available and complex to compute. Furthermore, the study presented in this chapter also showed the significance of the data for the data-driven method. In the battery pack temperature prediction study, the temperature prediction at the location not presented in the training data was less accurate. This shortcoming of the LSTM method leads to the PINN method to train the LSTM method with the collected data and the physics laws.

Chapter 3 proposes a PINN model to predict the lithium-ion battery cell temperature during the constant charge and discharge cycle. The PINN model was developed by applying the battery thermal model to the loss function, by implementing adaptive coefficients to the loss function, and by modifying the ANN architecture with the pre-layer and connection layer reflecting the analytical solution of the battery thermal model. The comparative study presented in this chapter indicated the superiority in predicting the lithium-ion battery cell temperature with limited data size and an unidentified battery thermal model.

In Chapter 4, an LSTM-PINN hybrid model was proposed to predict the lithium-ion battery pack temperatures. The proposed LSTM-PINN hybrid model has a unique PINN architecture to process the battery test data with chamber (ambient) temperature variation. When data scarcity occurs, the proposed LSTM-PINN hybrid model has more accurate predictions than the LSTM model proposed in Chapter 2. In this study, the geometric locations of the input battery temperature measurement and the predicted battery temperature are different, creating data scarcity. Furthermore, in the comparative study presented in this chapter, the proposed LSTM-PINN hybrid model showed robustness against the incompleteness of the battery thermal model, which includes missing terms and a less descriptive physics model.

Chapter 5 studied the effects of various data sampling methods for battery model parameter identification with LSTM. In the comparative study, PB, LH, and combined PB/LH sampling methods were reviewed and proposed to reduce the number of sample data for the training of the LSTM method while maintaining reasonable prediction accuracy. With the proposed sampling methods, the number of the battery parameters identified by the LSTM method will increase since the data produced by the battery model simulation are cost-effectively designed to include more battery model parameters while keeping a practically computable simulation data size.

6.2 Possible Future Extensions

This dissertation proposes data-driven approaches to estimate battery behaviors such as voltage and temperature. PINN effectively overcame the shortcomings of other data-driven approaches among the proposed data-driven approaches due to their dependency on the data to train the data-driven method. In the PINN method, physics laws and data are applied together to train the data-driven method. This dissertation implemented the PINN method to predict the battery temperature. Nevertheless, the following can be considered opportunities for future research to advance the presented work.

6.2.1 PINN for Lithium-Ion Battery Voltage Prediction

Lithium-ion battery voltage is another battery behavior that could be predicted by the PINN method. For PINN method implementation, less complex battery models such as ECM or single-particle model (SPM) could be implemented to support a data-driven model such as LSTM. There are a couple of improvements expected from the PINN implementation. First, a data-driven method like LSTM has a limited voltage prediction when the input variable has a profile with discontinuity, such as the sudden current pulse peak. This limitation is due to the local data scarcity at the discontinuity. The implementation of a PINN will improve this limitation as it does for the battery temperature prediction. Second, the output battery voltage prediction rate could be more flexible. In the case of the PINN method, the output prediction rate could be different from the training data sampling rate because the battery model trains the PINN to make the battery voltage predictions at a different rate from the training data sampling rate. Furthermore, for this future study, the PINN model will be trained with the actual vehicle driving profiles to analyze the proposed PINN model's prediction accuracy with the dynamic profiles.

6.2.2 PINN for Lithium-Ion Battery Mechanical Stress

Lithium-ion volume and mechanical stress changes are other lithium-ion battery behaviors that could be predicted by the PINN method. The volume changes due to electrode particle cracking, gas generation, and growth of the solid electrolyte interphase layer influence the battery capacity, power capability, and SOH [113]–[115]. With physical models describing the aging processes, the PINN method can predict the lithium-ion battery volume and mechanical stress changes and the contribution of the various aging processes.

Bibliography

[1] Liu, Dunnan, Xiaodan Guo, and Bowen Xiao. "What causes growth of global greenhouse gas emissions? Evidence from 40 countries." Science of the Total Environment 661 (2019): 750-766.

[2] Heede, Richard. "Tracing anthropogenic carbon dioxide and methane emissions to fossil fuel and cement producers, 1854–2010." Climatic change 122.1 (2014): 229-241.

[3] Reddy, Thomas B. Linden's handbook of batteries. McGraw-Hill Education, 2011.

[4] Zubi, Ghassan, et al. "The lithium-ion battery: State of the art and future perspectives." Renewable and Sustainable Energy Reviews 89 (2018): 292-308.

[5] Barsali, Stefano, Carmine Miulli, and Andrea Possenti. "A control strategy to minimize fuel consumption of series hybrid electric vehicles." IEEE Transactions on energy conversion 19.1 (2004): 187-195.

[6] Ehsani, Mehrdad, Khwaja M. Rahman, and Hamid A. Toliyat. "Propulsion system design of electric and hybrid vehicles." IEEE Transactions on industrial electronics 44.1 (1997): 19-27.

[7] Liu, Jinming, and Huei Peng. "Modeling and control of a power-split hybrid vehicle." IEEE transactions on control systems technology 16.6 (2008): 1242-1251.

[8] Wittmann, Jochen. "Electrification and digitalization as disruptive trends: new perspectives for the automotive industry?" Phantom Ex Machina. Springer, Cham, 2017. 137-159.

[9] "Useable Battery Capacity of Full Electric Vehicles Cheatsheet-EV Database." EV Database, https://ev-database.org/cheatsheet/useable-battery-capacity-electric-car. [Online; accessed 13-June-2022].

[10] Rao, Zhonghao, and Shuangfeng Wang. "A review of power battery thermal energy management." Renewable and Sustainable Energy Reviews 15.9 (2011): 4554-4571.

[11] Huggins, Robert. Advanced batteries: materials science aspects. Springer Science & Business Media, 2008.

[12] Raijmakers, L. H. J., et al. "A review on various temperature-indication methods for Li-ion batteries." Applied energy 240 (2019): 918-945.

[13] Kim, Jaewan, Jinwoo Oh, and Hoseong Lee. "Review on battery thermal management system for electric vehicles." Applied thermal engineering 149 (2019): 192-212.

[14] Tobishima, Shin-ichi, and Jun-ichi Yamaki. "A consideration of lithium cell safety." Journal of Power Sources 81 (1999): 882-886.

[15] Spotnitz, R., and J. Franklin. "Abuse behavior of high-power, lithium-ion cells." Journal of power sources 113.1 (2003): 81-100.

[16] Ouyang, Quan, et al. "Nonlinear observer design for the state of charge of lithium-ion batteries." IFAC Proceedings Volumes 47.3 (2014): 2794-2799.

[17] Hinton, Geoffrey E., and Ruslan R. Salakhutdinov. "Reducing the dimensionality of data with neural networks." science 313.5786 (2006): 504-507.

[18] Hinton, Geoffrey E., Simon Osindero, and Yee-Whye Teh. "A fast learning algorithm for deep belief nets." Neural computation 18.7 (2006): 1527-1554.

[19] Wu, Yu-chen, and Jun-wen Feng. "Development and application of artificial neural network." Wireless Personal Communications 102.2 (2018): 1645-1656.

[20] Zhang, Zhen, et al. "Real-time surface EMG pattern recognition for hand gestures based on an artificial neural network." Sensors 19.14 (2019): 3170.

[21] Baroni, Marco. "Linguistic generalization and compositionality in modern artificial neural networks." Philosophical Transactions of the Royal Society B 375.1791 (2020): 20190307.

[22] Sorin, Vera, et al. "Deep learning for natural language processing in radiology—fundamentals and a systematic review." Journal of the American College of Radiology 17.5 (2020): 639-648.

[23] Costantino, Francesco, Giulio Di Gravio, and Fabio Nonino. "Project selection in project portfolio management: An artificial neural network model based on critical success factors." International Journal of Project Management 33.8 (2015): 1744-1754.

[24] Refenes, Apostolos Nikolaos, and M. Azema-Barac. "Neural network applications in financial asset management." Neural Computing & Applications 2.1 (1994): 13-39.

[25] Amato, Filippo, et al. "Artificial neural networks in medical diagnosis." Journal of applied biomedicine 11.2 (2013): 47-58.

[26] Bakator, Mihalj, and Dragica Radosav. "Deep learning and medical diagnosis: A review of literature." Multimodal Technologies and Interaction 2.3 (2018): 47.

[27] Walczak, Steven. "An empirical analysis of data requirements for financial forecasting with neural networks." Journal of management information systems 17.4 (2001): 203-222.

[28] Hamid, Shaikh A., and Abraham Habib. "Financial forecasting with neural networks." Academy of Accounting and Financial Studies Journal 18.4 (2014): 37.

[29] Zou, Jinming, Yi Han, and Sung-Sau So. "Overview of artificial neural networks." Artificial Neural Networks (2008): 14-22.

[30] Kaelbling, Leslie Pack, Michael L. Littman, and Andrew W. Moore. "Reinforcement learning: A survey." Journal of artificial intelligence research 4 (1996): 237-285.

[31] D. Zhu, G. Cho and J. J. Campbell, "Neural Networks Battery Applications: A Review," 2021 IEEE International Conference on Electro Information Technology (EIT), 2021, pp. 1-8.

[32] Sharma, Sagar, Simone Sharma, and Anidhya Athaiya. "Activation functions in neural networks." towards data science 6.12 (2017): 310-316.

[33] Li, Lianlin, et al. "DeepNIS: Deep neural network for nonlinear electromagnetic inverse scattering." IEEE Transactions on Antennas and Propagation 67.3 (2018): 1819-1825.

[34] Eivazi, Hamidreza, et al. "Deep neural networks for nonlinear model order reduction of unsteady flows." Physics of Fluids 32.10 (2020): 105104.

[35] Qian, Lijun, Yuan Si, and Lihong Qiu. "SOC estimation of LiFePO4 Li-ion battery using BP Neural Network." EVS28 International Electric Vehicle Symposium and Exhibition. 2015.

[36] Chemali, Ephrem, et al. "State-of-charge estimation of Li-ion batteries using deep neural networks: A machine learning approach." Journal of Power Sources 400 (2018): 242-255.

[37] Hannan, Mahammad A., et al. "Neural network approach for estimating state of charge of lithium-ion battery using backtracking search algorithm." Ieee Access 6 (2018): 10069-10079.

[38] Lipu, MS Hossain, et al. "Optimal neural network approach for estimating state of energy of lithium-ion battery using heuristic optimization techniques." 2017 6th International Conference on Electrical Engineering and Informatics (ICEEI). IEEE, 2017.

[39] Chaoui, Hicham, and Chinemerem Christopher Ibe-Ekeocha. "State of charge and state of health estimation for lithium batteries using recurrent neural networks." IEEE Transactions on vehicular technology 66.10 (2017): 8773-8783.

[40] Yang, Duo, et al. "A neural network based state-of-health estimation of lithium-ion battery in electric vehicles." Energy Procedia 105 (2017): 2059-2064.

[41] Ren, Lei, et al. "Remaining useful life prediction for lithium-ion battery: A deep learning approach." Ieee Access 6 (2018): 50587-50598.

[42] De Sousa, Thais Tóssoli, et al. "Comparison of different approaches for lead acid battery state of health estimation based on artificial neural networks algorithms." 2016 IEEE Conference on Evolving and Adaptive Intelligent Systems (EAIS). IEEE, 2016.

[43] Eddahech, Akram, et al. "Behavior and state-of-health monitoring of Li-ion batteries using impedance spectroscopy and recurrent neural networks." International Journal of Electrical Power & Energy Systems 42.1 (2012): 487-494.

[44] Cho, Gyouho, Di Zhu, and Jeffrey Campbell. A Comparative Study of Recurrent Neural Network Architectures for Battery Voltage Prediction. No. 2021-01-1252. SAE Technical Paper, 2021.

[45] Zhu, Di, and Ewan Pritchard. NCSU year three final technical report. No. 2014-01-2907. SAE Technical Paper, 2014.

[46] Zhu, Di, et al. "Optimization of rule-based energy management strategies for hybrid vehicles using dynamic programming." Combust. Engines 184 (2021): 3-10.

[47] Zhao, Ruxiu, et al. "A compact unified methodology via a recurrent neural network for accurate modeling of lithium-ion battery voltage and state-of-charge." 2017 IEEE Energy Conversion Congress and Exposition (ECCE). IEEE, 2017.

[48] Hong, Jichao, Zhenpo Wang, and Yongtao Yao. "Fault prognosis of battery system based on accurate voltage abnormity prognosis using long short-term memory neural networks." Applied Energy 251 (2019): 113381.

[49] Li, Da, et al. "Battery fault diagnosis for electric vehicles based on voltage abnormality by combining the long short-term memory neural network and the equivalent circuit model." IEEE Transactions on Power Electronics 36.2 (2020): 1303-1315.

[50] “FreedomCAR Battery Test Manual For Power-Assist Hybrid Electric Vehicles.”, https://avt.inl.gov/sites/default/files/pdf/battery/freedomcar_manual_04_15_03.pdf. [Online; accessed 22-June-2022].

[51] Raijmakers, L. H. J., et al. "A review on various temperature-indication methods for Li-ion batteries." Applied energy 240 (2019): 918-945.

[52] Kim, Jaewan, Jinwoo Oh, and Hoseong Lee. "Review on battery thermal management system for electric vehicles." Applied thermal engineering 149 (2019): 192-212.

[53] Naguib, Mina, et al. "Accurate Surface Temperature Estimation of Lithium-Ion Batteries Using Feedforward and Recurrent Artificial Neural Networks." 2021 IEEE Transportation Electrification Conference & Expo (ITEC). IEEE, 2021.

[54] Ojo, Olaoluwa, et al. "A Recurrent Neural Networks Approach for Estimating the Core Temperature in Lithium-Ion Batteries."

[55] Capizzi, Giacomo, Francesco Bonanno, and Giuseppe M. Tina. "Recurrent neural network-based modeling and simulation of lead-acid batteries charge–discharge." IEEE Transactions on Energy Conversion 26.2 (2011): 435-443.

[56] Géron, Aurélien. Hands-on Machine Learning with Scikit-Learn, Keras, and TensorFlow: Concepts, Tools, and Techniques to Build Intelligent Systems. O'Reilly Media, Inc., 2019.

[57] Di Zhu, Gyouho Cho, Jeffrey Joseph Campbell. "Neural Networks Battery Applications: A Review." 2021 IEEE International Conference on Electro Information Technology (2021): 1-8.

[58] Chung, Junyoung, et al. "Empirical evaluation of gated recurrent neural networks on sequence modeling." arXiv preprint arXiv:1412.3555 (2014).

[59] Campbell, Jeffrey, Di Zhu, and Gyouho Cho. Estimation of Surface Temperature Distributions Across an Array of Lithium-Ion Battery Cells Using a Long Short-Term Memory Neural Network. No. 2022-01-0713. SAE Technical Paper, 2022.

[60] Chollet, Francois. Deep learning with Python. Simon and Schuster, 2021.

[61] Karniadakis, George Em, et al. "Physics-informed machine learning." Nature Reviews Physics 3.6 (2021): 422-440.

[62] Raissi, Maziar, Paris Perdikaris, and George E. Karniadakis. "Physics-informed neural networks: A deep learning framework for solving forward and inverse problems involving nonlinear partial differential equations." Journal of Computational physics 378 (2019): 686-707.

[63] Raissi, Maziar, Paris Perdikaris, and George Em Karniadakis. "Physics informed deep learning (part i): Data-driven solutions of nonlinear partial differential equations." arXiv preprint arXiv:1711.10561 (2017).

[64] Mao, Zhiping, Ameya D. Jagtap, and George Em Karniadakis. "Physics-informed neural networks for high-speed flows." Computer Methods in Applied Mechanics and Engineering 360 (2020): 112789.

[65] Sun, Luning, et al. "Surrogate modeling for fluid flows based on physics-constrained deep learning without simulation data." Computer Methods in Applied Mechanics and Engineering 361 (2020): 112732.

[66] Raissi, Maziar, Alireza Yazdani, and George Em Karniadakis. "Hidden fluid mechanics: Learning velocity and pressure fields from flow visualizations." Science 367.6481 (2020): 1026-1030.

[67] Jin, Xiaowei, et al. "NSFnets (Navier-Stokes flow nets): Physics-informed neural networks for the incompressible Navier-Stokes equations." Journal of Computational Physics 426 (2021): 109951.

[68] Almajid, Muhammad M., and Moataz O. Abu-Al-Saud. "Prediction of porous media fluid flow using physics informed neural networks." Journal of Petroleum Science and Engineering 208 (2022): 109205.

[69] Vahab, Mohammad, et al. "A physics informed neural network approach to solution and identification of biharmonic equations of elasticity." arXiv preprint arXiv:2108.07243 (2021).

[70] Henkes, Alexander, Henning Wessels, and Rolf Mahnken. "Physics informed neural networks for continuum micromechanics." Computer Methods in Applied Mechanics and Engineering 393 (2022): 114790.

[71] Bharadwaja, B. V. S. S., et al. "Physics-Informed Machine Learning and Uncertainty Quantification for Mechanics of Heterogeneous Materials." arXiv preprint arXiv:2202.10423 (2022).

[72] Jiang, Xiaotian, et al. "Physics-informed neural network for nonlinear dynamics in fiber optics." arXiv preprint arXiv:2109.00526 (2021).

[73] Zang, Yubin, et al. "Principle-Driven Fiber Transmission Model Based on PINN Neural Network." Journal of Lightwave Technology 40.2 (2021): 404-414.

[74] Wang, Danshi, et al. "Applications of Physics-Informed Neural Network for Optical Fiber Communications." IEEE Communications Magazine (2022).

[75] Rad, M. Torabi, et al. "Theory-training deep neural networks for an alloy solidification benchmark problem." Computational Materials Science 180 (2020): 109687.

[76] Zobeiry, Navid, and Keith D. Humfeld. "A physics-informed machine learning approach for solving heat transfer equation in advanced manufacturing and engineering applications." Engineering Applications of Artificial Intelligence 101 (2021): 104232.

[77] Niaki, Sina Amini, et al. "Physics-informed neural network for modelling the thermochemical curing process of composite-tool systems during manufacture." Computer Methods in Applied Mechanics and Engineering 384 (2021): 113959.

[78] Zhao, Xiaoyu, et al. "Physics-informed Convolutional Neural Networks for Temperature Field Prediction of Heat Source Layout without Labeled Data." arXiv preprint arXiv:2109.12482 (2021).

[79] Liu, Xu, et al. "Temperature field inversion of heat-source systems via physics-informed neural networks." Engineering Applications of Artificial Intelligence 113 (2022): 104902.

[80] Irrgang, Christopher, et al. "Towards neural Earth system modelling by integrating artificial intelligence in Earth system science." Nature Machine Intelligence 3.8 (2021): 667-674.

[81] Lu, Lu, et al. "DeepXDE: A deep learning library for solving differential equations." SIAM Review 63.1 (2021): 208-228.

[82] Hennigh, Oliver, et al. "NVIDIA SimNet™: An AI-accelerated multi-physics simulation framework." International Conference on Computational Science. Springer, Cham, 2021.

[83] Haghighat, Ehsan, and Ruben Juanes. "Sciann: A keras/tensorflow wrapper for scientific computations and physics-informed deep learning using artificial neural networks." Computer Methods in Applied Mechanics and Engineering 373 (2021): 113552.

[84] Araz, Jack Y., Juan Carlos Criado, and Michael Spannowsky. "Elvet--a neural network-based differential equation and variational problem solver." arXiv preprint arXiv:2103.14575 (2021).

[85] McClenny, Levi D., Mulugeta A. Haile, and Ulisses M. Braga-Neto. "TensorDiffEq: Scalable Multi-GPU Forward and Inverse Solvers for Physics Informed Neural Networks." arXiv preprint arXiv:2103.16034 (2021).

[86] Koryagin, Alexander, Roman Khudorozkov, and Sergey Tsimfer. "PyDEns: A python framework for solving differential equations with neural networks." arXiv preprint arXiv:1909.11544 (2019).

[87] Chen, Feiyu, et al. "Neurodiffeq: A python package for solving differential equations with neural networks." Journal of Open Source Software 5.46 (2020): 1931.

[88] Zubov, Kirill, et al. "NeuralPDE: Automating physics-informed neural networks (PINNs) with error approximations." arXiv preprint arXiv:2107.09443 (2021).

[89] Wight, Colby L., and Jia Zhao. "Solving allen-cahn and cahn-hilliard equations using the adaptive physics informed neural networks." arXiv preprint arXiv:2007.04542 (2020).

[90] Wang, Sifan, Yujun Teng, and Paris Perdikaris. "Understanding and mitigating gradient flow pathologies in physics-informed neural networks." SIAM Journal on Scientific Computing 43.5 (2021): A3055-A3081.

[91] Wang, Sifan, Xinling Yu, and Paris Perdikaris. "When and why PINNs fail to train: A neural tangent kernel perspective." Journal of Computational Physics 449 (2022): 110768.

[92] Liu, Dehao, and Yan Wang. "A Dual-Dimer method for training physics-constrained neural networks with minimax architecture." Neural Networks 136 (2021): 112-125.

[93] McClenny, Levi, and Ulisses Braga-Neto. "Self-adaptive physics-informed neural networks using a soft attention mechanism." arXiv preprint arXiv:2009.04544 (2020).

[94] Lin, Xinfan, et al. "Robust estimation of battery system temperature distribution under sparse sensing and uncertainty." IEEE Transactions on Control Systems Technology 28.3 (2019): 753-765.

[95] Soltani, Mahdi, et al. "A Three-dimensional thermal model for a commercial lithium-ion capacitor battery pack with non-uniform temperature distribution." 2019 IEEE International Conference on Industrial Technology (ICIT). IEEE, 2019.

[96] Iraola, Unai, et al. "Influence of voltage balancing on the temperature distribution of a Li-ion battery module." IEEE Transactions on Energy Conversion 30.2 (2014): 507-514.

[97] Chen, Siqi, et al. "A thermal design and experimental investigation for the fast-charging process of a lithium-ion battery module with liquid cooling." Journal of Electrochemical Energy Conversion and Storage 17.2 (2020).

[98] Coman, Paul T., et al. "A Reduced-Order Lumped Model for Li-Ion Battery Packs during Operation." Journal of The Electrochemical Society 168.10 (2021): 100525.

[99] Bernardi, D., E. Pawlikowski, and John Newman. "A general energy balance for battery systems." Journal of the electrochemical society 132.1 (1985): 5.

[100] Park, S., Kato, D., Gima, Z., Klein, R. and Moura, S., 2018. Optimal experimental design for parameterization of an electrochemical lithium-ion battery model. Journal of The Electrochemical Society, 165(7), p.A1309.

[101] Schmidt, A.P., Bitzer, M., Imre, Á.W. and Guzzella, L., 2010. Experiment-driven electrochemical modeling and systematic parameterization for a lithium-ion battery cell. Journal of Power Sources, 195(15), pp.5071-5080.

[102] Forman, J.C., Moura, S.J., Stein, J.L. and Fathy, H.K., 2012. Genetic identification and fisher identifiability analysis of the Doyle–Fuller–Newman model from experimental cycling of a LiFePO4 cell. Journal of Power Sources, 210, pp.263-275.

[103] Vazquez-Arenas, J., Gimenez, L.E., Fowler, M., Han, T. and Chen, S.K., 2014. A rapid estimation and sensitivity analysis of parameters describing the behavior of commercial Li-ion batteries including thermal analysis. Energy Conversion and Management, 87, pp.472-482.

[104] Jokar, A., Rajabloo, B., Desilets, M. and Lacroix, M., 2017. An On-line Electrochemical Parameter Estimation Study of Lithium-Ion Batteries Using Neural Networks. Ecs Transactions, 75(20), p.73.

[105] Turetskyy, A., Laue, V., Lamprecht, R., Thiede, S., Krewer, U. and Herrmann, C., 2019, July. Artificial Neural Network enabled P2D Model Deployment for End-of-Line Battery Cell Characterization. In 2019 IEEE 17th International Conference on Industrial Informatics (INDIN) (Vol. 1, pp. 53-58). IEEE.

[106] Chun, H., Kim, J. and Han, S., 2019. Parameter identification of an electrochemical lithium-ion battery model with convolutional neural network. IFAC-PapersOnLine, 52(4), pp.129-134.

[107] Chun, H., Kim, J., Yu, J. and Han, S., 2020. Real-time parameter estimation of an electrochemical lithium-ion battery model using a long short-term memory network. IEEE Access, 8, pp.81789-81799.

[108] Devore, Jay L. Probability and Statistics for Engineering and the Science. Duxbury, 1995.

[109] Huntington, D.E. and Lyrintzis, C.S., 1998. Improvements to and limitations of Latin hypercube sampling. Probabilistic engineering mechanics, 13(4), pp.245-253.

[110] Chang-Hui Chen, Ferran Brosa Planella, Kieran O'Regan, Dominika Gastol, W. Dhammika Widanage, and Emma Kendrick. "Development of Experimental Techniques for Parameterization of Multi-scale Lithium-ion Battery Models." Submitted for publication (2020).

[111] A. Nyman, M. Behm, and G. Lindbergh, "Electrochemical characterisation and modelling of the mass transport phenomena in LiPF6-EC-EMC electrolyte," Electrochim. Acta, vol. 53, no. 22, pp. 6356–6365, 2008.

[112] Kim, G. H., Smith, K., Lee, K. J., Santhanagopalan, S., & Pesaran, A. (2011). Multi-domain modeling of lithium-ion batteries encompassing multi-physics in varied length scales. Journal of The Electrochemical Society, 158(8), A955-A969.

[113] Cho, J., Kim, Y. J., Kim, T. J., & Park, B. (2001). Zero-strain intercalation cathode for rechargeable Li-Ion cell. Angewandte Chemie, 113(18), 3471-3473.

[114] Cannarella, John, and Craig B. Arnold. "Stress evolution and capacity fade in constrained lithium-ion pouch cells." Journal of Power Sources 245 (2014): 745-751.

[115] Ersal, T., Brudnak, M., Salvi, A., Stein, J. L., Filipi, Z., & Fathy, H. K. (2011). Development and model-based transparency analysis of an Internet-distributed hardware-in-the-loop simulation platform. Mechatronics, 21(1), 22-29.